

## Competition between magnetic interactions and structural instabilities leading to itinerant frustration in the triangular lattice antiferromagnet $\text{LiCrSe}_2$

Elisabetta Nocerino<sup>1</sup>✉, Shintaro Kobayashi<sup>2</sup>, Catherine Witteveen<sup>3,4</sup>, Ola K. Forslund<sup>5</sup>, Nami Matsubara<sup>1</sup>, Chiu Tang<sup>6</sup>, Takeshi Matsukawa<sup>7</sup>, Akinori Hoshikawa<sup>7</sup>, Akihiro Koda<sup>8,9</sup>, Kazuyoshi Yoshimura<sup>10</sup>, Izumi Umegaki<sup>11</sup>, Yasmine Sassa<sup>5</sup>, Fabian O. von Rohr<sup>3</sup>, Vladimir Pomjakushin<sup>12</sup>, Jess H. Brewer<sup>13,14</sup>, Jun Sugiyama<sup>15,16</sup> & Martin Månsson<sup>1</sup>✉

$\text{LiCrSe}_2$  constitutes a recent valuable addition to the ensemble of two-dimensional triangular lattice antiferromagnets. In this work, we present a comprehensive study of the low temperature nuclear and magnetic structure established in this material. Being subject to a strong magnetoelastic coupling,  $\text{LiCrSe}_2$  was found to undergo a first order structural transition from a trigonal crystal system ( $P\bar{3}m1$ ) to a monoclinic one ( $C2/m$ ) at  $T_s = 30$  K. Such restructuring of the lattice is accompanied by a magnetic transition at  $T_N = 30$  K. Refinement of the magnetic structure with neutron diffraction data and complementary muon spin rotation analysis reveal the presence of a complex incommensurate magnetic structure with a up-up-down-down arrangement of the chromium moments with ferromagnetic double chains coupled antiferromagnetically. The spin axial vector is also modulated both in direction and modulus, resulting in a spin density wave-like order with periodic suppression of the chromium moment along the chains. This behavior is believed to appear as a result of strong competition between direct exchange antiferromagnetic and superexchange ferromagnetic couplings established between both nearest neighbor and next nearest neighbor  $\text{Cr}^{3+}$  ions. We finally conjecture that the resulting magnetic order is stabilized via subtle vacancy/charge order within the lithium layers, potentially causing a mix of two co-existing magnetic phases within the sample.

<sup>1</sup>KTH Royal Institute of Technology, Department of Applied Physics, Alba Nova University Center, Stockholm SE-114 21, Sweden. <sup>2</sup>Japan Synchrotron Radiation Research Institute (JASRI), 1-1-1 Kouto, Sayo 679-5198, Japan. <sup>3</sup>Department of Quantum Matter Physics, University of Geneva, 24 Quai Ernest-Ansermet, 1211 Geneva, Switzerland. <sup>4</sup>Department of Physics, University of Zürich, Winterthurerstr. 190, 8057 Zürich, Switzerland. <sup>5</sup>Chalmers University of Technology, Department of Physics, Göteborg SE-412 96, Sweden. <sup>6</sup>Diamond House, Harwell Science and Innovation Campus, Fermi Ave, Didcot OX11 0DE, UK. <sup>7</sup>Frontier Research Center for Applied Atomic Sciences, Ibaraki University, 162-1 Shirakata, Tokai, Ibaraki 319-1106, Japan. <sup>8</sup>Muon Science Laboratory, Institute of Materials Structure Science, High Energy Accelerator Research Organization (KEK), Tokai, Ibaraki 319-1106, Japan. <sup>9</sup>Department of Materials Structure Science, The Graduate University for Advanced Studies, Tsukuba, Ibaraki 305-0801, Japan. <sup>10</sup>Department of Chemistry, Graduate School of Science, Kyoto University, Kyoto 606-8502, Japan. <sup>11</sup>Muon Science Laboratory, Institute of Materials Structure Science, KEK, Tokai, Ibaraki 319-1106, Japan. <sup>12</sup>Laboratory for Neutron Scattering and Imaging, Paul Scherrer Institute, 5232 Villigen, PSI, Switzerland. <sup>13</sup>Department of Physics and Astronomy, University of British Columbia, Vancouver, BC V6T 1Z1, Canada. <sup>14</sup>TRIUMF, 4004 Wesbrook Mall, Vancouver, BC V6T 2A3, Canada. <sup>15</sup>Neutron Science and Technology Center, Comprehensive Research Organization for Science and Society (CROSS), Tokai, Ibaraki 319-1106, Japan. <sup>16</sup>Advanced Science Research Center, Japan Atomic Energy Agency, Tokai, Ibaraki 319-1195, Japan. ✉email: [nocerino@kth.se](mailto:nocerino@kth.se); [condmat@kth.se](mailto:condmat@kth.se)

In periodic crystalline lattices containing magnetic atoms, long-range ordering of their electronic magnetic moments can be stabilized by the exchange couplings among them at low temperatures. In some systems however, due to peculiar structural properties, not all these interactions can be satisfied simultaneously. Examples of such systems are provided by geometrically frustrated triangular lattice antiferromagnets (TLA), whose crystal structure consists of two-dimensional triangular lattice (2D-TL) layers, in which each corner of the triangular lattice is occupied by a magnetic atom, with nearest neighbor antiferromagnetic (AFM) interactions that cannot be stabilized<sup>1</sup>. Some prominent representative cases of 2D-TLA are found amid transition metal oxides (TMO), such as  $\text{NaCoO}_2$ <sup>2-7</sup> or  $\text{Li/Na/KCrO}_2$ <sup>8,9</sup>. The highly degenerate spin states established in these materials, owing to their inherent geometrical frustration, may result in diverse exotic magnetic ground states and electronic properties. Indeed, due to subtle differences between one system and another, as well as to the strong interplay established between their lattice geometry and correlated electrons, these materials can host anomalous orbital states<sup>10-12</sup>, unconventional superconductivity<sup>13,14</sup>, rare magnetic ground states<sup>15-17</sup>, and distinctive spin-lattice dynamics<sup>18-20</sup>. The latter two aspects will be the main focus of this work. Among the currently available 2D-TLA, chromium-based compounds of the type  $\text{ACrX}_2$ , where A is a monovalent atom and X is a chalcogen element, have been extensively investigated as geometrically frustrated  $S = 3/2$  Heisenberg spin systems. The interest around these materials lies in the fact that they manifest a smörgåsbord of complex magnetic ground states<sup>19,21-27</sup> and attractive technological properties (e.g. multiferroicity)<sup>28-30</sup>. These systems entail higher energy spin configurations, therefore, in the low-temperature regime, often a compromise between spin and lattice degrees of freedom has to be reached. The compromise can be realized through a first-order energetically beneficial distortion of the lattice leading to a new symmetry of the crystal, in which new interaction paths are realized and a magnetic order can be stabilized. When such an interplay between strongly correlated spins and geometrical degrees of freedom is realized, it is said that the system manifests magnetoelastic coupling. The appeal for materials undergoing these kinds of phenomena is twofold, as they constitute a unique playground for fundamental scientific research<sup>19,21-27,31</sup>, but also lend themselves to potential future technical applications<sup>32,33</sup>. Here it is worth mentioning that, in the context of quantum magnetism and magnetic frustration,  $S = 1/2$  is often considered the theoretically ideal spin configuration, being the smallest non-integer spin value allowing for non-trivial quantum behavior.  $S = 3/2$  systems involve larger spin values compared to  $S = 1/2$ , which can lead to a richer and more complex physics due to stronger magnetic interactions and quantum fluctuations, but also to a more challenging theoretical landscape to explore. Therefore, while theoretical modeling remains beneficial for guiding experimental investigations and providing qualitative insights, experimental studies on existing materials are crucial to ultimately clarify the physics of  $S = 3/2$  systems.

The recent synthesis of  $\text{LiCrSe}_2$ , via Li intercalation in  $\text{CrSe}_2$  by Kobayashi et al.<sup>34,35</sup>, constitutes a valuable addition to the ensemble of TLAs that manifest magnetoelastic coupling since, probably due to the difficulty in manufacturing alkali chromium selenides, the most of the studies in this framework are performed on oxides and sulfides. Beyond the fundamental physics interest surrounding  $\text{LiCrSe}_2$ , recent theoretical works foresee remarkable electronic properties, such as the presence of tunable field-free topological spin textures, which make this material appealing for applications in spintronics circuitry<sup>36-38</sup>. The room-temperature crystal structure of  $\text{LiCrSe}_2$  was identified as trigonal by synchrotron X-ray diffraction, with space group  $P3m1$ . Here, the

$\text{Cr}^{3+}$  ions create 2DTL layers, stacked along the  $c$  axis, by the connection of edge-sharing  $\text{CrSe}_6$  octahedra in the  $ab$ -plane<sup>39</sup>. Indications of a first-order structural transition towards a lower symmetry crystal system were observed around  $T = 30$  K with in-house X-ray diffraction<sup>35</sup>; here it is suggested that such transition leads to a low temperature monoclinic structure. From bulk magnetic characterization methods,  $\text{LiCrSe}_2$  was found to undergo a first order-like magnetic transition, with an AFM character, also around  $T_N = 30$  K, which is a hint of magnetoelastic coupling. This behavior is similar to the one observed in the magnetoelastic TLA-Cr sulfides  $\text{AuCrS}_2$  and  $\text{AgCrS}_2$ <sup>22,26</sup>. However, remarkable qualitative differences in the structural distortions and magnetic properties between  $\text{LiCrSe}_2$  and the sulfides, indicate that  $\text{LiCrSe}_2$  would select a different magnetic ground state with respect to the one realized in  $\text{AuCrS}_2$  and  $\text{AgCrS}_2$ . Indeed, the small negative value of the  $\text{LiCrSe}_2$  Curie-Weiss temperature  $\Theta = -28$  K and the small frustration index  $f = \frac{|\Theta|}{T_N} \approx 1$  estimated in reference<sup>35</sup>, are suggestive of a weak nearest neighbor magnetic interaction (weaker than the one found in the sulfides) in favor of a strong further neighbor magnetic interaction (stronger than the one found in the sulfides). These results indicate that further neighbor interactions have a leading role in the determination of the magnetic ground state in  $\text{LiCrSe}_2$ , making it a promising candidate for the realization of unconventional magnetic structures.

In this work, we investigated the temperature evolution of the crystal and magnetic structure of polycrystalline  $\text{LiCrSe}_2$  by means of neutron diffraction (ND), synchrotron X-ray diffraction (XRD) and muon spin rotation ( $\mu^+$ SR). Our observations confirm the conjectures of Kobayashi and coworkers<sup>35</sup>, as a clear structural transition from trigonal to monoclinic crystal system is observed and a complex incommensurate magnetic structure seems to be established in the sample, with periodic modulation in direction and modulus of the  $\text{Cr}^{3+}$  spin axial vector. Here we identified a main magnetic structure and a possible magnetic superstructure which contribute differently to the neutron diffraction pattern, suggesting that one is larger than the other, as also indicated by the  $\mu^+$ SR analysis. A solution for the main and secondary magnetic structures is proposed, together with a possible interpretation of such a spin ordering in terms of the magnetic exchange interactions for the main phase.

## Results

**Muon spin rotation experiment.** A zero-field (ZF) and weak transverse field (wTF) bulk  $\mu^+$ SR experiment has been performed for different temperatures, in order to observe the evolution of the sample's internal magnetic field distribution. In the wTF mode an external magnetic field of weak magnitude is applied (here, wTF = 30 G), with its flux lines perpendicular to the initial direction of the muon spin polarization. In this set-up, it is possible to follow the magnetic phase transition, while lowering the temperature of the system, as the muon spin precession (Larmor precession) is more and more affected by the sample's strong internal field, induced by long-range magnetic ordering, at the expense of the externally applied weak field (for more details about the  $\mu^+$ SR experimental technique refer to ref. 40).

The wTF time spectra are well fitted using the following function:

$$A_0 P_{\text{TF}}(t) = A_{\text{TF}} \cos\left(2\pi\nu_{\text{TF}}t + \frac{\pi\phi}{180}\right) \cdot e^{(-\lambda_{\text{TF}}t)} + A_{\text{tail}} \cdot e^{(-\lambda_{\text{tail}}t)} \quad (1)$$

where  $A_0$  is the initial asymmetry at time zero,  $P_{\text{TF}}(t)$  is the muon spin polarization function,  $A_{\text{TF}}$  is the oscillating asymmetry while  $A_{\text{tail}}$  is the asymmetry of a slow relaxing exponential term due to

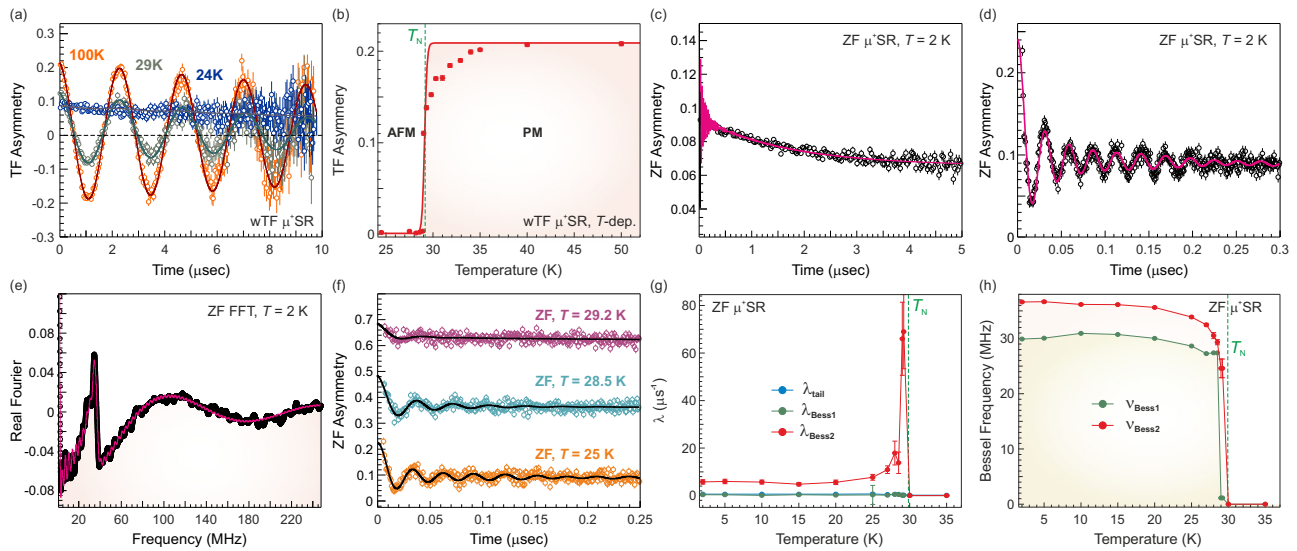


**Fig. 1 Results of the  $\mu^+$ SR analysis for  $\text{LiCrSe}_2$ .** **a** Weak transverse field (wTF)  $\mu^+$ SR time spectra at the selected temperatures 100 K (open orange circles), 29 K (open gray circles), 24 K (open blue circles). The best fit to the data (corresponding to the function in Eq. (1)) is shown as solid lines. **b** Temperature dependence of the wTF asymmetry (filled red circles), the continuous red line represents a fit to a sigmoid function giving the AFM transition temperature  $T_N = 29.11 \pm 0.06$  K. **c, d** Zero-field (ZF)  $\mu^+$ SR time spectrum at  $T = 2$  K (open black circles) with the fit to Eq. (2) (solid magenta line) shown in **(c)** long and **(d)** short time domain, respectively. **e** Fast Fourier Transform (FFT) of the spectrum and its fit shown in **(d)**. **f** ZF muon time spectra at selected temperatures  $T = 25$  K (orange open circles), 28.5 K (light blue open circles) and 29.2 K (purple open circles) in the short time domain. The spectra are shifted along the y-axis for clarity of display. The black continuous lines are fits to Eq. (2). **g, h** Temperature dependencies of the ZF fit parameters extracted from Eq. (2) for the two oscillating components of the signal (green and red filled circles) plus the slow tail component (blue filled circles). The error bars in the plot represent the confidence intervals of the reported values.

the components of the internal field which are parallel to the initial polarization direction of the muons spins. This “tail” component, is also sometimes called the “powder average” signal when measuring polycrystalline (powder) samples, which ideally constitute 1/3 of the total asymmetry (in our case  $A_{\text{tail}} \sim 0.08 \sim 0.22/3$  where the total asymmetry is equal to 0.22). Further,  $\nu_{\text{TF}}$  is the muon spin precession frequency having the phase  $\phi$  (which in this case has a value of  $\approx 12^\circ$  in the entire temperature range), and finally  $\lambda_{\text{TF}}$  and  $\lambda_{\text{tail}}$  are the depolarization rates for the respective polarization components. wTF  $\mu^+$ SR time spectra at selected temperatures are shown in Fig. 1a with best fits Eq. (1) as solid lines. Further fitting of the full wTF temperature dependence and extracting the wTF asymmetry as a function of temperature ( $A_{\text{TF}}(T)$ ), allow us to estimate the magnetic transition temperature of  $\text{LiCrSe}_2$ . The result is shown in Fig. 1b where  $A_{\text{TF}}(T)$  is fitted to a sigmoid function. Such a curve is commonly used in the  $\mu^+$ SR related research to follow the temperature dependence of magnetic transitions in magnetically ordered systems. Here the transition temperature  $T_N$  can be identified in correspondence with the inflection point of the s-shaped function, giving  $T_N = 29.11 \pm 0.06$  K, which is in very good agreement with previously published bulk characterizations<sup>35</sup>. From the wTF data, it is also possible to deduce that more or less 100% of the sample enters the magnetically ordered state. Further, and contrary to our previous  $\mu^+$ SR studies of the related  $\text{LiCrTe}_2$  compound<sup>41</sup>, we do not seem to have any clear missing asymmetry fraction above  $T_N$ , i.e. absence of any evident FM impurities in the current  $\text{LiCrSe}_2$  sample.

In the ZF configuration, the muon spin only senses the local internal magnetic field of the sample and if long-range magnetic order is established, a clear precession signal (i.e., oscillation) will appear. The ZF  $\mu^+$ SR time spectrum at base temperature ( $T = 2$  K) in  $\text{LiCrSe}_2$  is displayed in Fig. 1c, d.

At first look, the ZF signal in the short-time domain [Fig. 1d] presents very clear oscillations, indicating the occurrence of AFM

spin order. However, initial fitting attempts, using two simple exponentially relaxing cosine functions, gave poor results. Several problems were found, e.g., the full asymmetry could not be recovered, the fit could only work if the phase of the cosine functions would be left free and acquire very large un-physical values, and the chosen model could not fully capture the features of the Fast Fourier transformed (FFT) signal [Fig. 1e]. After testing several combinations of different oscillatory functions, the best fit to the data was achieved with a combination of two spherical Bessel functions  $j_0$ :

$$A_0 P_{\text{ZF}}(t) = A_{\text{Bess1}} j_0 \left( 2\pi\nu_{\text{Bess1}} t + \frac{\pi\phi_{\text{Bess1}}}{180} \right) \cdot e^{-\lambda_{\text{Bess1}} t} + A_{\text{Bess2}} j_0 \left( 2\pi\nu_{\text{Bess2}} t + \frac{\pi\phi_{\text{Bess2}}}{180} \right) \cdot e^{-\lambda_{\text{Bess2}} t} + A_{\text{tail}} \cdot e^{-\lambda_{\text{tail}} t} + A_{\text{BG}} \cdot e^{-\lambda_{\text{BG}} t}. \quad (2)$$

Here  $A_0$  is the initial asymmetry,  $P_{\text{ZF}}(t)$  is the muon spin polarization function,  $A_{\text{Bess1}}$  and  $A_{\text{Bess2}}$  are the asymmetries of the oscillating part of the signal,  $A_{\text{BG}}$  is a small background component possibly coming from muons stopping in the sample holder, and  $A_{\text{tail}}$  is the asymmetry of the tail component. The frequency of the Larmor precession is given by  $2\pi \cdot \nu_{\text{Bess}}$ , and  $\phi$  is the relative phase of the oscillating signals. Here  $\phi \approx 0$  for both the Bessel functions in the entire temperature range. Finally,  $\lambda_{\text{Bess}}$ ,  $\lambda_{\text{BG}}$ , and  $\lambda_{\text{tail}} = 0$  are the depolarization rates for the respective polarization components. Figure 1d, f shows the ZF raw data in the short time domain, for different temperatures, with the fitting curves as solid lines. As seen from these results, as well as the accurate fit to the FFT at  $T = 2$  K in a large frequency range in Fig. 1e, Eq. (2) provides a good model for the experimental data.

The temperature dependence of the relevant ZF fitting parameters is shown in Fig. 1g, h. For both the relaxation rates ( $\lambda$ ) as well as oscillation frequencies ( $\nu_{\text{Bess}}$ ) it is clear that an abrupt, first-order like, transition occurs for  $T_N \approx 30$  K. In more detail, the depolarization rate, and especially  $\lambda_{\text{Bess2}}$  display a very typical and



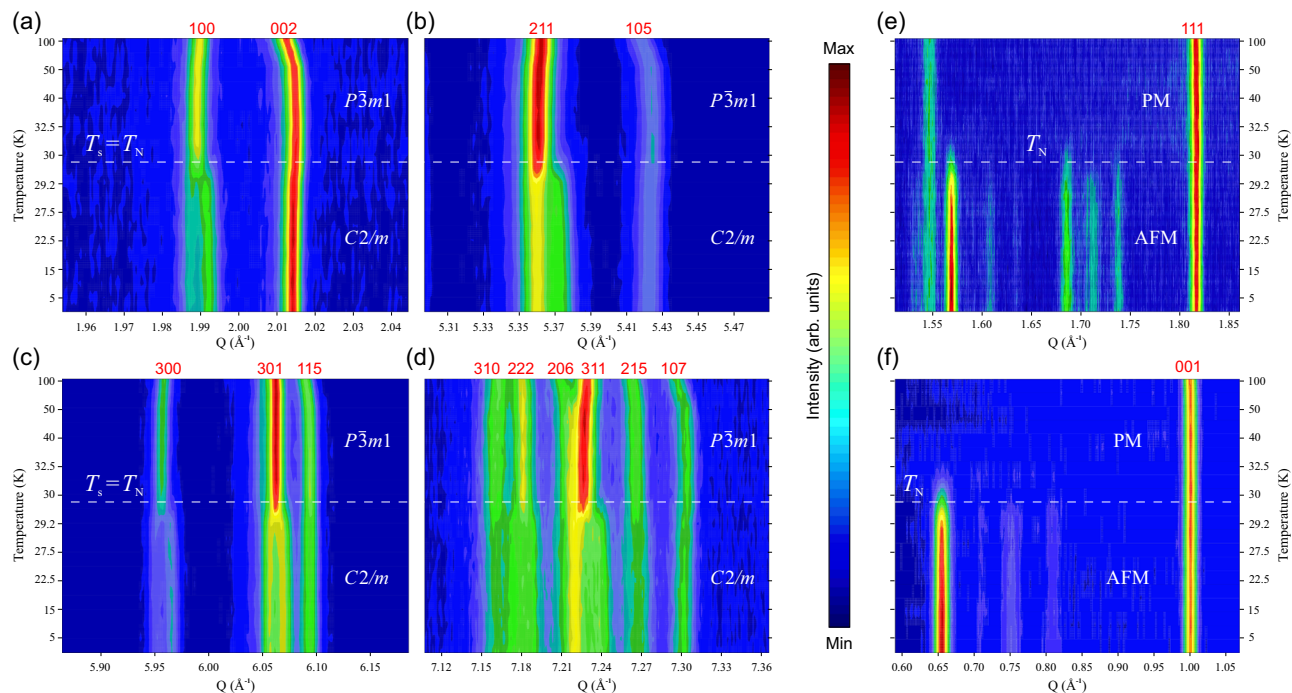


**Fig. 2** 2D color maps showing the temperature evolution of the NPD data for  $\text{LiCrSe}_2$ . **a–d** The nuclear Bragg peak splitting in different  $Q$  ranges below  $T_s \approx 30$  K indicates the structural phase transition from  $P\bar{3}m1$  to  $C2/m$ . **e, f** Magnetic Bragg peaks, plotted together with some (non splitted) nuclear peaks, appear below  $T_N \approx 30$  K. Please note the nonlinear temperature scale (y-axis), having a higher density of points in proximity of the transition, and that  $T_s = T_N$ . The Miller indices of the reflections in the high-temperature structure are reported in red for clarity of display.

strong increase just below  $T_N$ , indicating the onset of spin dynamics/fluctuations as the magnetic phase transition approaches. The trend for  $\lambda_{\text{Bess1}}$  is similar, however, the absolute values are much smaller. Here it is also important to emphasize that  $A_{\text{Bess2}} \approx 12 \cdot A_{\text{Bess1}}$ , i.e. the oscillating component Bess2 has more than an order of magnitude larger volume fraction with respect to Bess1. What such differences mean is hard to rigorously deduce using the  $\mu^+$ SR data alone. Nevertheless, it indicates that the two oscillating components originate from muons experiencing two rather different local magnetic environments<sup>42–44</sup>. Finally, the temperature dependence of the oscillation frequencies is shown in Fig. 1h, which reflect the magnetic order parameter of the phase transition. The behavior of the two components is in fact very similar, the oscillation frequencies have similar values, and follow the same temperature dependence. The latter shows an approximately constant trend below  $T_N$ , with a slow downturn of both  $\nu_{\text{Bess1}}$  and  $\nu_{\text{Bess2}}$ . This is then abruptly interrupted at  $T_N \approx 30$  K which, we know from previous studies<sup>35</sup>, coincides with a structural phase transition at  $T_s$ .

The presence of large non-zero phases ( $\phi$ ) for cosine functions and replacement with a damped  $j_0$  Bessel is commonly used in the  $\mu^+$ SR community to model incommensurate magnetic structures. This solution is well established and proven, both theoretically and experimentally, to describe incommensurate spin density waves associated with single  $q$ -vectors<sup>45–47</sup>. The presence of two distinct Bessel functions with two frequencies of similar value in  $\text{LiCrSe}_2$  could be due to the presence of two different muon-stopping sites in the lattice, thereby probing the same incommensurate magnetic structure in a different fashion. Another option would be that we have two slightly different incommensurate magnetic phases present in the sample. Additional discussions on this matter will follow below.

**Structural refinement from X-ray and neutron powder diffraction.** The high- and low-temperature crystal structure of

$\text{LiCrSe}_2$ , was determined from high-resolution neutron powder diffraction (NPD) studies [see Fig. 2a–f and Fig. 3c–f] along with complementary synchrotron X-ray diffraction (XRD) data [see Fig. 3a, b]. The refinement of the diffraction patterns was carried out by means of the Rietveld refinement method. Here we adopted a global refinement routine, which simultaneously included the three detector banks BS, SE, and LA35 covering the high-, intermediate-, and low- $Q$  regions, respectively. The atomic positions, the cell parameters, and the basis vectors of the magnetic moment were refined as common parameters among the 3 data files. The calculated NPD/XRD pattern consists of a majority  $\text{LiCrSe}_2$  phase plus a small  $\text{Li}_2\text{Se}$  non-magnetic impurity phase (the  $\text{Li}_2\text{Se}$  impurity weight fraction in the diffraction pattern is 1.5%, consistently with the  $\mu^+$ SR data). For the XRD an additional Al phase is included to account for the sample holder/capillary. Further, for NPD the magnetic phase is present below  $T_N$  in the low  $Q$ -range, while disregarded for large  $Q$  due to the magnetic form factor<sup>48</sup> (by means of the command MDLIM in FullProf).

The room temperature crystal structure [see Fig. 3g] was found to be well modeled by the trigonal  $P\bar{3}m1$  space group (no. 164), with lattice parameters  $a = b = 3.65425(3)$  Å,  $c = 6.28911(4)$  Å,  $\alpha = \beta = 90^\circ$ ,  $\gamma = 120^\circ$ , in which  $\text{Cr}^{3+}$  ions occupy the vertices of the hexagonal unit cell, hereby creating the 2D-TLA. Below  $T \approx 30$  K (corresponding to both the structural and magnetic transition temperatures  $T_s = T_N$ ), the diffraction pattern undergoes a dramatic change, as clearly displayed in Fig. 2. Several nuclear Bragg peaks split into double peaks [Fig. 2(a–d)] and, at the same time, the magnetic Bragg peaks appear [Fig. 2e, f]. Concerning the structural change, the increased number of Bragg reflections in the diffraction pattern, due to the peak splitting, is suggestive of a symmetry loss in the system, possibly owing to the disappearance of the 3-fold symmetry axis of the high-temperature parent space group. Moreover, no clear superlattice reflection peaks seem to appear in the experimental data.

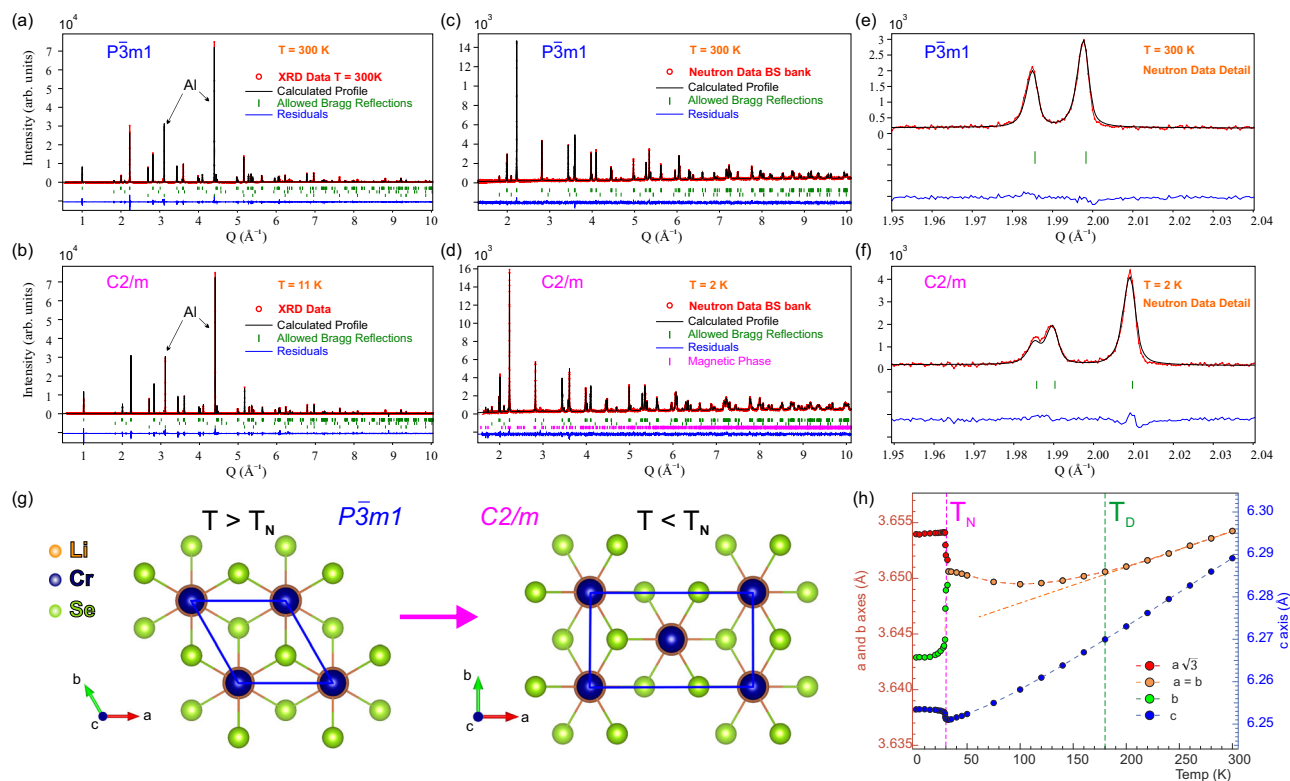


**Fig. 3 Results of the XRD and NPD structural investigation of  $\text{LiCrSe}_2$ .** **a, b** X-ray diffraction patterns (red circles) with the corresponding calculated patterns (black continuous line) resulting from structural refinement at room and base temperature. **c–f** Neutron diffraction patterns (high-Q detector bank BS) with the corresponding calculated patterns resulting from structural refinement at room and base temperature. The peak splitting is clearly visible in the close-up plot in **(f)**. **g** Graphic representation of the crystal structure in polycrystalline  $\text{LiCrSe}_2$  at 300 K and 2 K oriented along the  $c$  axis for clear visualization of the  $ab$ -plane. **h** Temperature dependence of the lattice parameters  $a = b$  (orange filled circles),  $c$  (blue filled circles) in  $\text{LiCrSe}_2$ . The  $y$ -axis of the lattice parameter  $c$  is plotted on the right for clarity of display. The values of the lattice parameters below the transition (where  $a$  and  $b$  are represented with red and green filled circles respectively) are reported in the hexagonal setting for correct comparison with the higher temperature values. The dashed lines are guides to the eye. The error bars in the plot represent the confidence intervals of the reported values.

Under the light of these observations, and from a group/subgroup relationship argument, the most probable final space group for such a structural transition would be the monoclinic  $C2/m$  (no. 12). This is because  $C2/m$  is the only monoclinic maximal subgroup of the parent space group  $P\bar{3}m1$  with a single step in its symmetry reduction path (see Bärnighausen tree for  $P\bar{3}m1$  from the Bilbao Crystallographic Server<sup>49</sup>). Indeed, Rietveld refinement of the low-temperature diffraction pattern with  $C2/m$  provided a good agreement with the experimental data, as it was able to correctly index all the additional new peaks [Fig. 3b, d, f]. Nevertheless, in light of the first-order nature of the structural transition, the possibility that the group subgroup relationship might not hold in this particular case must be considered. Several other monoclinic space groups were tested with a trial an error approach; among them  $Cm$  (no. 8) provided the best matching between the calculated and the observed pattern, which was however comparable to  $C2/m$ . The fact that the loss of the 2-fold symmetry axis from  $C2/m$  to  $Cm$  did not improve the refinement, made  $C2/m$  a more reasonable choice. This space group was also suggested from previous in-house XRD measurements<sup>35</sup>, and we have now confirmed such suggestion with high-resolution experimental methods. The base temperature ( $T = 2$  K) crystal structure was therefore modeled with the monoclinic  $C2/m$  space group, with lattice parameters  $a = 6.32904(8)$  Å,  $b = 3.64287(5)$  Å,  $c = 6.25345(7)$  Å,  $\alpha = \gamma = 90^\circ$ , and  $\beta = 90.08(13)^\circ$  (see also the crystallographic information file provided as Supplementary Data 1–3). Here the  $\text{Cr}^{3+}$  ions occupy the vertices of a unit

cell, which is nearly rectangular in the  $ab$ -plane, with one additional Cr atom in the central point of coordinates  $(0.5, 0.5, z)$  [see Fig. 3g]. The detailed result of the refinement is displayed in Fig. 3(e, f), with a plot of the observed and calculated diffraction patterns at high and low temperature, in the high-resolution high-Q BS detector bank. It is important to emphasize that in this bank (and  $Q$ -range) any potential low-temperature magnetic peak is virtually invisible, and does not interfere with the structural refinement. The complementary XRD patterns are also shown [Fig. 3a, b], and the structural refinement for XRD/NPD measurements is fully consistent, further allowing us to effectively discern between nuclear and magnetic contributions. It should also be noted that refinement of fractional occupancies did not improve the goodness of the fit, which allows us to conclude that the  $\text{LiCrSe}_2$  sample has a stoichiometric composition very close to the ideal one.

The temperature evolution of the lattice parameters, resulting from the structural refinement, is displayed in Fig. 3h. Table 1 further summarizes the refined structural parameter along with the Bragg agreement  $R$  factors, whose low values highlight the goodness of the refinement model. Since the Cr atoms sit at the vertices of the unit cell, the evolution of the lattice parameters reflects directly the evolution of the in-plane Cr–Cr distances. This is a factor of major importance in the determination of the magnetic structure for 2D-TLAs<sup>50</sup>. On cooling, the size of the crystallographic axes is reduced, due to thermal contraction, down to the magnetic transition temperature  $T_N$ . As seen in

**Table 1 Structural parameters.**

	300 K	2 K
Space Group	$P\bar{3}m1$	$C2/m$
$a$ Å	3.65425(3)	6.32904(8)
$b$ Å	3.65425(3)	3.64287(5)
$c$ Å	6.28911(4)	6.25345(7)
$\alpha$	90°	90°
$\beta$	90°	90.0762(13)°
$\gamma$	120°	90°
Li ( $x, y, z$ )	(0, 0, $\frac{1}{2}$ )	(0, 0, $\frac{1}{2}$ )
Cr ( $x, y, z$ )	(0, 0, 0)	(0, 0, 0)
Se ( $x, y, z$ )	( $\frac{1}{3}, \frac{2}{3}, 0.226(1)$ )	(0.667(3), 0, 0.773(1))
$B_{Li}$ (Å <sup>2</sup> )	1.98(9)	0.85(7)
$B_{Cr}$ (Å <sup>2</sup> )	0.63(5)	0.23(3)
$B_{Se}$ (Å <sup>2</sup> )	0.39(1)	0.018(7)
$R_{B(nuc)}$ (%)	4.2	4.5

Lattice parameters, atomic positions, isotropic thermal displacement parameters and Bragg  $R$  factors from refinement of neutron powder diffraction data on polycrystalline LiCrSe<sub>2</sub>

Fig. 3h, the contraction of the  $c$ -axis occurs at a much higher rate with respect to the  $a$ - and  $b$ -axes, which is phenomenologically compatible with the 2D-TLA nature of the compound. At  $T_N = T_s$  the first-order structural transition is clearly visible as a sharp change in the temperature dependence of the axes, with the major effect observed in the  $ab$ -plane. The synchronized nuclear and magnetic phase transition appearing at  $T = 30$  K indicated a strong spin-lattice coupling. Here, the ordering of the Cr magnetic moments seems to be the driving mechanism for such a modification of the crystal lattice, aimed at stabilizing the competing coupling mechanisms simultaneously established among them. To further clarify such synergic effect, a detailed understanding of the spin structure is required. A dedicated discussion around the structural evolution of the system in concomitance with the evolution of the magnetic structure will be presented in the next subsection.

**Magnetic refinement from neutron powder diffraction.** Several temperature-dependent magnetic Bragg peaks appear below 30 K, as clearly seen in Fig. 2e, f. These peaks are assumed to be magnetic. Such transition is presented in higher detail in Fig. 4a, b, which displays a comparison between NPD patterns (intermediate- $Q$  SE  $\rightarrow$  90° and low- $Q$  LA35  $\rightarrow$  35° detector banks) acquired at  $T = 35$  K (just above  $T_N$ ) and at base temperature ( $T = 2$  K). The square root of the integrated intensity of the large magnetic peak in the lower  $Q$ -region ( $Q = 0.66 \text{ \AA}^{-1}$ ) is also plotted as a function of temperature [see Fig. 4c]. The latter quantity reflects the order parameter of the magnetic transition which, as clearly seen from the plot in Fig. 4c, has a first-order character. The fit of the plot to a sigmoid function [solid line in Fig. 4c], well follows the sharp profile of the data and provides the magnetic transition temperature  $T_N = 29.94 \pm 0.09$  K (defined as the midpoint of the sigmoid curve). The inset of Fig. 4c shows the normalized integrated intensities of the large magnetic peak together with the two neighboring small satellites, which all clearly manifest the same temperature-dependent behavior. Nevertheless, as discussed further below, these peaks do not belong to the same magnetic phase. Here a distinction is necessary between a *main* and a *secondary* magnetic phase. In the immediate following, we will describe the main magnetic phase.

The magnetic propagation vector  $\mathbf{q}_{\text{main}}$  was determined by a very extensive trial and error procedure with the software K-Search. As expected from our  $\mu^+$ SR data, it was found to be incommensurate:  $\mathbf{q}_{\text{main}} = (0.045, \approx \frac{1}{4}, \approx \frac{1}{2})$ , see also Table 2 for

the exact values. Such propagation vector can successfully index the high-intensity magnetic peak and most of the lower intensity ones as well. The origin of the remaining un-indexed weak peaks [e.g. at  $Q = 0.74 \text{ \AA}^{-1}$ , orange arrow in Fig. 4a] will be discussed in the next section.

The Rietveld Method was used to refine the LiCrSe<sub>2</sub> magnetic ( $\mathbf{q}_{\text{main}}$ ) phase. This phase includes a single magnetic Cr atom in the crystallographic site Cr(0 0 0). To ensure an accurate estimation of the Cr magnetic moment  $\mu_{\text{Cr}}$ , the scale factor and structural parameters were constrained to match their counterparts in the nuclear LiCrSe<sub>2</sub> phase. The software Baslreps provided only one possible irreducible representation of the propagation vector group  $G_k$  for  $\mathbf{q}_{\text{main}}$ , compatible with the space group  $C2/m$  (IRrep  $\Gamma_1$ ), consisting of three basis vectors BsV, with no imaginary components, parallel to the main crystallographic axes:

- BsV(1): Re (1 0 0),
- BsV(2): Re (0 1 0),
- BsV(3): Re (0 0 1).

The refinement of the coefficients of the basis vectors C1, C2 and C3, representing here the weights of the basis vectors in the decomposition of the projections of the spin axial vector along the main crystallographic axes<sup>51</sup>, provided a large component along the  $a$  direction and a negligibly small component along the  $b$  direction [Fig. 5a–g].

Using IRrep  $\Gamma_1$  in the magnetic structure refinement [shown in Fig. 5a–d], it was possible to capture the temperature-dependent magnetic peaks of the diffraction pattern indexed by the  $q$ -vector  $\mathbf{q}_{\text{main}}$ . The resulting magnetic structure presents a very large magnetic unit cell, with AFM coupled layers stacked along the  $c$ -axis with a peculiar “breathing” arrangement of the moments within the  $ab$ -plane [Fig. 5e–g]. Such arrangement of the spins resembles a spin-density wave-like structure, but without angular modulation of the Cr spin axial vector and with a very long periodicity. The intra-layer orientation of the Cr moments along the  $b$ -axis is reminiscent of an alternate up-up-down-down sequence [see dashed magenta ellipses in Fig. 5g], built up by double FM-coupled Cr spin chains running along the  $a$ -axis. This peculiar arrangement of the Cr moments is very similar to what was found for AuCrS<sub>2</sub><sup>22</sup>. However, in this case the orientation of the spins in the FM-coupled chains undergoes a change of direction, accompanied by a size modulation of the magnetic moment while moving along the  $a$ -axis [see plot (e) and bottom of panel (g) in Fig. 5]. As a result, a periodic suppression of the magnetic moment appears along the chain. The modulation interval between two consecutive spin flips along the  $a$ -axis is 11 unit cells. Figure 5e, f displays the calculated value of the Cr moment  $\mu_{\text{Cr}}$  as a function of the atomic coordinate  $x_{\text{Cr}}$ . This is obtained as the modulus of the refined spin axial vector expressed in units of Bohr magneton. The periodic “breathing” feature of the magnetic moment modulation is clearly visible. The simple 22-cell periodicity displayed in Fig. 5 is referred to a single one-dimensional Cr chain running along the  $a$ -axis for clarity of display. Given the incommensurate three-dimensional propagation vector of this magnetic structure, no simple periodicity for the orientation of the Cr spins can be identified in three dimensions.

The highest value for  $\mu_{\text{Cr}}$  in the chain is  $2.25(3)\mu_B$ , lower than the value previously estimated from bulk magnetic measurements  $\approx 4 \mu_B$ <sup>35</sup>, which is closer to the ideal spin-only value  $\mu_{3/2} = 2\sqrt{S(S+1)} = 3.87 \mu_B$  for an isolated Cr<sup>3+</sup> ion in the spin state  $S = 3/2$ . This discrepancy is likely due to the differences between the two investigation methods. For a transition metal element in a covalently bonded system, a lower value of its magnetic moment with respect to the ideal value is expected, due to the competition



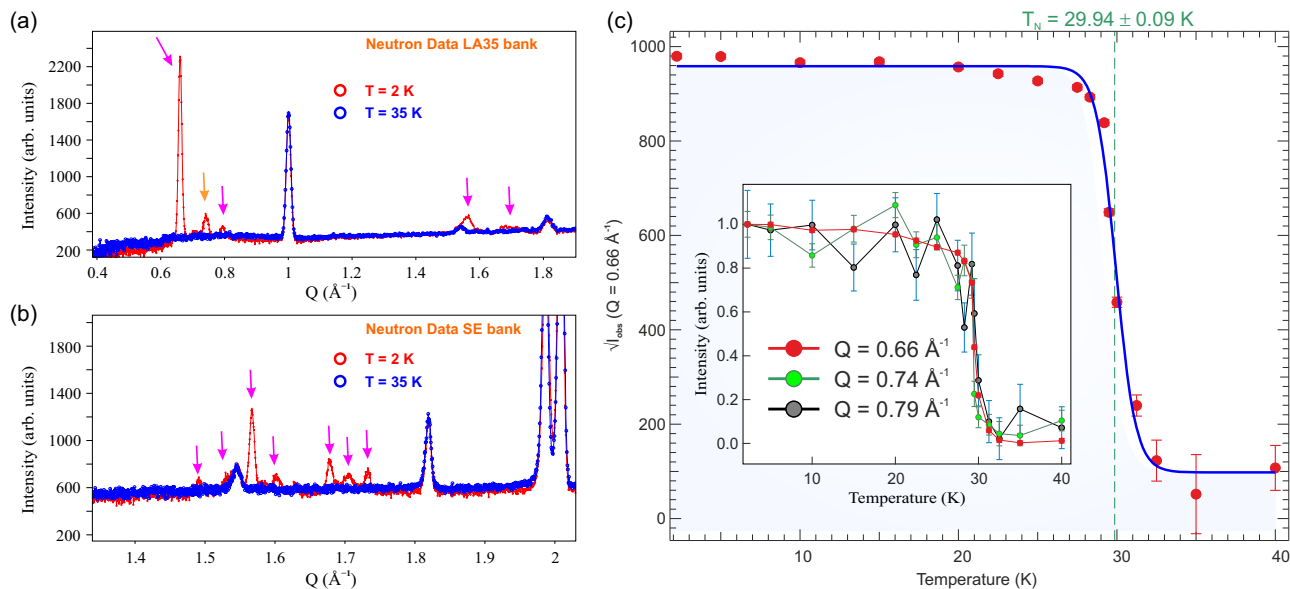


**Fig. 4** Temperature dependence of the magnetic features in the NPD raw data for  $\text{LiCrSe}_2$ . Neutron diffraction patterns at  $T = 35$  K (blue open circles) and  $T = 2$  K (red open circles) acquired using the (a) low-Q LA35 and (b) intermediate-Q SE detector banks, respectively. The appearance of magnetic Bragg peaks below  $T_N \approx 30$  K is evidenced by the magenta arrows (orange arrow indicates the strongest among the peaks left un-indexed by the main magnetic phase). **c** Square root of the integrated intensity of the strongest magnetic peak at  $Q = 0.66 \text{ \AA}^{-1}$  (red filled circles), visible in the low-Q LA35 Bank. The continuous line is a fit to a sigmoid function for precise determination of the magnetic transition temperature. The inset shows the  $Q = 0.66 \text{ \AA}^{-1}$  normalized integrated intensity together with the other two lowest  $Q$  magnetic peaks for comparison,  $Q = 0.74 \text{ \AA}^{-1}$  (green filled circles) and  $Q = 0.79 \text{ \AA}^{-1}$  (gray filled circles). The error bars in the plot represent the confidence intervals of the reported values.

**Table 2** Main Magnetic Phase parameters.

**Space Group:**  $\overline{C}1$

$a_m$ (Å)	75.9486(1)
$b_m$ (Å)	14.57148(2)
$c_m$ (Å)	12.50691(2)
$\alpha_m$	90°
$\beta_m$	90.0762(13)°
$\gamma_m$	90°
Magnetic atom	Cr
Wyckoff site	2a
$\mathbf{q}_{\text{main}}$	0.0453(1), 0.2508(2), 0.5009(4)
$R_{B(\text{mag})}$ (%)	2.91
$\mu_{\text{Cr}}$ ( $\mu_B$ )	2.25(3)

Magnetic refinement parameters and agreement factors for the neutron powder diffraction data from  $\text{LiCrSe}_2$  at  $T = 2$  K.

between covalency and magnetism<sup>52</sup>. This reduction would occur at low temperature, where the system is in the ordered state. On the other hand, effective moments at high temperature, in the paramagnetic region, are not necessarily reduced<sup>53</sup>, hence the value estimated in reference<sup>35</sup>. Further, when geometric frustration is present, the appearance of staggered magnetic moments and a following reduction of  $\mu_{\text{Cr}}$  is very common<sup>8,22,26,54–56</sup>. Therefore, frustration might also be a contributor to the low-temperature reduction of the effective Cr moment in  $\text{LiCrSe}_2$ . As also mentioned above, the frustration index in  $\text{LiCrSe}_2$  was also estimated in reference<sup>35</sup> as  $f = \frac{|\mathbf{Q}|}{T_N} \approx 1$ . Such value would imply the absence of frustration in this system. However, in the presence of simultaneously co-existing FM and AFM intralayer interactions such as in this case, the Weiss temperature does not directly reflect the magnitude of antiferromagnetic interactions, which may lead to an underestimation of the frustration index. Such behavior was recently observed also in  $\text{AgCrSe}_2$ <sup>57</sup>, a compound that manifests in many aspects a phenomenology

similar to  $\text{LiCrSe}_2$ . Therefore, in agreement with systems analogous to  $\text{LiCrSe}_2$ <sup>22</sup>, the value  $\mu_{\text{Cr}} = 2.25(3)\mu_B$  estimated by NPD in the current work can be considered reliable, and consistent with a  $S = 3/2$  spin system scenario. The resulting parameters obtained from the refinement of the magnetic unit cell for the  $\text{LiCrSe}_2$  magnetic phase are reported in Table 2. The very good agreement between the observed profiles and the calculated models can be clearly seen in Fig. 5(a-d). The goodness of the model is confirmed by the low value of the reliability  $R$ -factor for the magnetic phase, also reported in Table 2, not exceeding a few percent. All the values reported in Tables 1 and 2 are obtained from the global, simultaneous Rietveld refinement of diffraction patterns from the 3 detector banks BS, SE and LA35 covering the high-, intermediate-, and low- $Q$  regions respectively. Although in powder diffraction studies possible ambiguities in the indexing of the magnetic peaks can eventuate, the analysis method used here (i.e., extremely high-resolution high- $Q$  diffraction patterns are refined in a global routine together with the low- $Q$  diffraction patterns, where the peaks from the magnetic structures can be clearly detected) ensures the reliability of our solution.

**High-temperature properties.** Concerning the high-temperature structural and dynamic properties of  $\text{LiCrSe}_2$ , the refined isotropic thermal displacement parameters  $B_{\text{iso}}$  up to 400 K are shown in Fig. 6a. Here, the structural transition at  $T_N = 30$  K is clearly visible. It can be seen that  $B_{\text{iso}}$  for all atoms actually deviate from the general trend already above the transition. The first detectable temperature point where the refined Debye–Waller factors for all the atoms in the lattice abruptly move away from their trend at higher temperatures is regarded as the temperature point indicating the onset of a structural instability (si):  $T_{\text{si}} \approx 45$  K. This would also explain the broad transition found in the wTF  $\mu^+\text{SR}$  data [Fig. 1(b)], just above the first-order downturn. It is also clear that the Li atoms undergo the largest thermal displacement (cf. Cr and Se). At high temperature  $B_{\text{Li}}$  display an

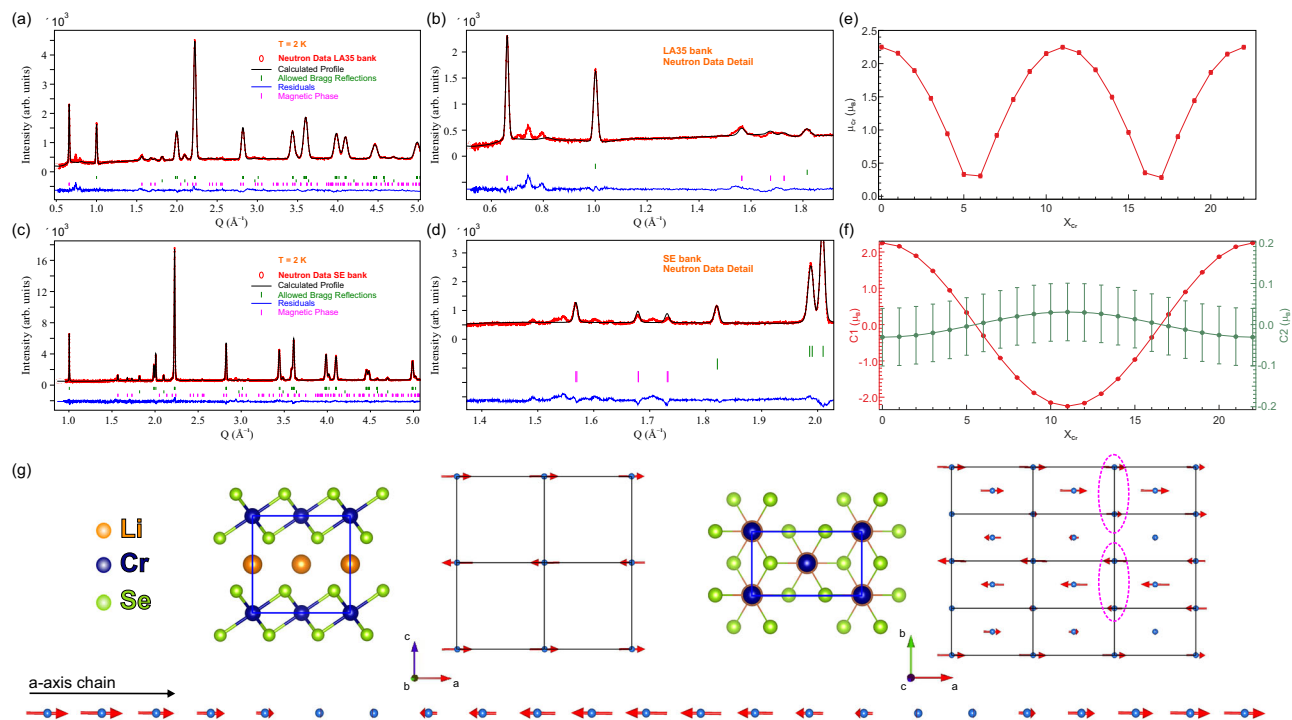


**Fig. 5** NPD results for the Main Magnetic Phase in LiCrSe<sub>2</sub>. Overview and close-up neutron diffraction pattern measured at  $T = 2$  K (red circles) with the corresponding calculated pattern resulting from magnetic refinement (black continuous line) using the (a, b) low-Q LA35 and (c, d) intermediate-Q SE, detector banks, respectively. e Value of the spin only Cr moment and (f) the components of the axial spin vector C1 (left y-axis red filled circles) and C2 (right y-axis gray filled circles). Both plotted along the  $a$ -axis as a function of the  $x_{Cr}$  atomic coordinate. g Graphic representation of the main magnetic structure in polycrystalline LiCrSe<sub>2</sub> oriented along the main axes of the unit cell (4 cells in the  $ac$ -plane, 12 cells in the  $ab$ -plane, and finally 22 cells along the  $a$ -axis at the very bottom). The up-up-down-down arrangement of the spins along the  $b$ -axis is highlighted by the dashed magenta ellipses. See also Table 2 for refined parameters. The error bars in the plot represent the confidence intervals of the reported values.

almost linear temperature dependence, however, below approximately 180 K a clear deviation from this trend appears. If we consider the similarity of LiCrSe<sub>2</sub> with several other well-known layered TMO compounds (e.g. LiCoO<sub>2</sub><sup>58</sup>), and their utilization in rechargeable batteries<sup>59</sup>, we should consider the possibility of, and effects from, Li-ion dynamics. In fact, our team has developed and pioneered an experimental method to investigate ion dynamics by  $\mu^+$ SR. A detailed description of the method and selected examples can be found in refs. 60–62. Briefly, the muon spin is so sensitive to internal fields that it is capable of even probing static and dynamic changes in the nuclear moment. When implanted in these compounds in their higher temperature paramagnetic (PM) phase, the muon will mainly ‘feel’ the nuclear moment of the alkali metal (here Li), measured in both ZF and applied magnetic field parallel to the initial direction of the muon spin polarization (LF- $\mu^+$  + SR). If the Li-ion is static, only a static nuclear field distribution ( $\Delta$ ) is probed. However, if Li-ion dynamics sets in, an additional field fluctuation rate ( $\nu$ ) component will be present. In the simplest interpretation,  $\nu$  would translate into a Li-ion hopping rate that can be directly probed as a function of, e.g. temperature. In fact, our team recently conducted initial test measurements (still to be completed) of Li-ion dynamics in LiCrSe<sub>2</sub> at the instrument S1 in J-PARC (see the Methods section for further experimental details) and  $\nu(T)$  was successfully extracted at a few selected temperatures. As shown in Fig. 6(b),  $\nu(T)$  displays a clear exponential trend, typical for a thermally activated diffusion process, where the exponential curve starts to move away from its horizontal asymptote around  $T_D \approx 180$  K. This means that the Li-ions are fully mobile at least down to  $T_D \approx 180$  K, which would indicate the possibility for Li order to appear during cool-down of the sample. This would also explain

the change of trend found for  $B_{Li}$  at  $T_D$ . In fact, a smaller kink is also visible in  $B_{Se}$ , which is reasonable considering that the Se sits next to the Li layers in the LiCrSe<sub>2</sub> structure [see inset of Fig. 6b]. Interestingly, this behavior is different with respect to the one observed in the directly related compound LiCrO<sub>2</sub>, which was proven to be electrochemically inactive up to 480 K, despite its striking structural similarity with LiCrSe<sub>2</sub>. Therefore, the diffusion properties of this material could provide a hint on how to increment the Li-ion mobility in layered structures.

## Discussion

The low-temperature incommensurate magnetic order, with itinerant frustration of the Cr moment<sup>63,64</sup>, found in LiCrSe<sub>2</sub> is rather peculiar. While the inter-planar magnetic ordering along the  $c$ -axis can be explained with an AFM coupling mediated by super-exchange interactions through the path Cr-Se-Se-Cr, to explain the complex intra-planar magnetic structure the coexistence of competing magnetic interactions must be considered. In ternary chromium chalcogenide compounds, the magnetic interactions between two neighboring Cr<sup>3+</sup> ions can be of two types, as for the Goodenough–Kanamori–Anderson rules<sup>65–67</sup>. Either a FM super-exchange interaction is established, by hybridization of the  $p$  orbitals of the  $d$  orbitals of the Cr ions (specifically with the half-filled  $t_{2g}$  orbital of one Cr ion and the empty  $e_g$  orbital of the other one) forming a 90° bond of the type Cr–Anion–Cr; or an AFM direct exchange interaction is established between the half-filled  $t_{2g}$  orbitals of two adjacent Cr<sup>3+</sup> ions. In the FM coupling, the Cr–Cr distance  $d(\text{Cr–Cr})$  is unimportant as long as the angle in the bond Cr–Anion–Cr is close to 90°. On the other hand, for the AFM coupling,  $d(\text{Cr–Cr})$



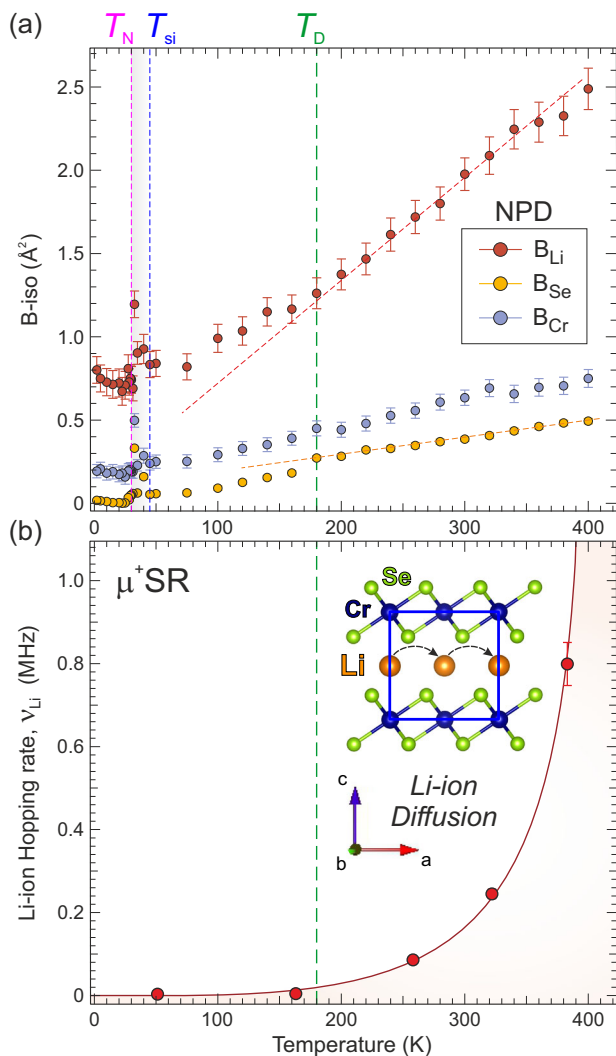


**Fig. 6** High temperature properties of LiCrSe<sub>2</sub> investigated with NPD and LF- $\mu^+$ SR analysis. **a** Temperature dependence of the isotropic Debye-Waller factors  $B_{\text{iso}}$  for the Li (red filled circles), Cr (violet filled circles), and Se (yellow filled circles) atoms from NPD data. **b** Temperature dependence of the Li-ion hopping rate ( $\nu_{\text{Li}}$ ) from  $\mu^+$ SR measurements. Inset in **(b)** shows the layered structure where Li-ions diffuse (hop) from site to site above  $T_D \approx 180$  K.  $T_{\text{si}} \approx 45$  K indicates the onset of the structural instability. Solid and dashed lines are guides to the eye. The error bars in the plots represent the confidence intervals of the reported values.

has a major relevance. Rosenberg and coworkers identified a cutoff nearest neighbor (NN) Cr–Cr distance of  $\approx 3.6$   $\text{\AA}$  in the Cr layers of ternary chromium chalcogenides, for one mechanism to be dominant over the other<sup>50</sup>. In particular, for  $d(\text{Cr}–\text{Cr}) < 3.6$   $\text{\AA}$  the AFM interaction would be preferred, while for  $d(\text{Cr}–\text{Cr}) > 3.6$   $\text{\AA}$  the FM interaction would be preferred. In LiCrSe<sub>2</sub> a dramatic structural change is observed, in concomitance to the magnetic transition at  $T_N$ , leading to a modification of the Cr–Cr distances and of the angles  $\text{Cr}–\widehat{\text{Se}}–\text{Cr}$ , which are summarized in Table 3. In the trigonal phase just above the magnetic transition, the distance  $\text{NN}–d(\text{Cr}–\text{Cr})_{a-b}$  is very close to the critical value 3.6  $\text{\AA}$  and the angle  $\text{Cr}–\widehat{\text{Se}}–\text{Cr}$  is very close to 90°. In these conditions, the AFM and FM couplings are equally likely to be established between NN Cr<sup>3+</sup> ions. As a consequence, the system is subjected to a geometrical frustration, which is removed through the energetically beneficial structural transition. This

**Table 3** Atomic distances and angles.

	35 K	2 K
Space Group	$P3m1$	$C2/m$
NN- $d_1(\text{Cr}–\text{Cr})_{a-b}$ ( $\text{\AA}$ )	3.65059(1)	3.64287(6)
NN- $d_2(\text{Cr}–\text{Cr})_{a-b}$ ( $\text{\AA}$ )	-	3.65128(4)
NNN- $d_1(\text{Cr}–\text{Cr})_{a-b}$ ( $\text{\AA}$ )	6.32301(1)	6.31449(7)
NNN- $d_2(\text{Cr}–\text{Cr})_{a-b}$ ( $\text{\AA}$ )	-	6.32905(9)
$d(\text{Cr}–\text{Cr})_c$ ( $\text{\AA}$ )	6.25113(1)	6.25345(8)
$\text{Cr}–\widehat{\text{Se}}–\text{Cr}_1$	91.8863(1)°	91.66(5)°
$\text{Cr}–\widehat{\text{Se}}–\text{Cr}_2$	91.8863(1)°	91.92(3)°

NN and NNN Cr–Cr distances and Cr–Se–Cr bonding angles just above and below the magnetic transition in LiCrSe<sub>2</sub>.

results in two non-equivalent NN and two non-equivalent next nearest neighbor (NNN) Cr<sup>3+</sup> distances,  $d_1(\text{Cr}–\text{Cr})_{a-b}$  and  $d_2(\text{Cr}–\text{Cr})_{a-b}$ . In the low-temperature monoclinic phase small distortions of the lattice occur, indeed both the NN distances are still very close to the critical value 3.6  $\text{\AA}$  (see Table 3), and the angles  $\text{Cr}–\widehat{\text{Se}}–\text{Cr}$  are still very close to 90°. Nevertheless, as usually happens in frustration-driven structural transitions, this distortion is enough to lift the degeneracy of the magnetic ground state. Here, a strong competition between AFM and FM interactions is established, which leads to an overall weakening of the exchange mechanism between NN Cr<sup>3+</sup> ions. At this point, the NNN Cr<sup>3+</sup> interactions must come into play to stabilize the magnetic structure. The alignment of the Cr moments, resulting from our magnetic refinement [Fig. 5], and the aforementioned structural considerations on the Cr bonds, are consistent with the presence of both in-plane FM and AFM interactions simultaneously established across NN ( $J_1$ ) and NNN ( $J_2$ ) Cr bonds. Based on these assumptions, a potential arrangement of the magnetic couplings in this system is proposed in Supplementary Fig. 1. In addition, exchange interaction established among further than NNN Cr ions might be relevant in the determination of the ground state of LiCrSe<sub>2</sub>. Indeed, it was found that in delafossite structures with S as chalcogenide ligand (e.g., AuCrS<sub>2</sub> and AgCrS<sub>2</sub>), the NNN exchange interaction  $J_2$  is typically comparable with the 3rd neighbor AFM exchange interaction  $J_3$ <sup>68</sup>. Such mechanism of super-super-exchange, realized via two  $p$ -orbitals of the S ligands, seems to drive the magnetic transition and determine the magnetic ground state in these materials<sup>68</sup>. The third neighbor interaction was recently found to be relevant also for the determination of the magnetic ground state in the triangular Cr-oxide PdCrO<sub>2</sub><sup>69</sup>. The  $p$ -orbitals of the Se element have a larger spatial extension with respect to the ones in S and O. Therefore, in qualitative agreement with the aforementioned systems<sup>68,69</sup>,  $J_3$  could be expected to be even larger than  $J_2$  in LiCrSe<sub>2</sub>. However, first principles calculations would be needed to ultimately ascertain the roles of  $J_1$ ,  $J_2$  and  $J_3$  in the determination of the magnetic order on this material.

The resulting magnetic structure presents ferromagnetic double chains running along the  $a$ -axis, which are AFM coupled along the  $b$ -axis, similarly to AuCrS<sub>2</sub> and AgCrS<sub>2</sub><sup>22,26</sup>. The only difference is that for LiCrSe<sub>2</sub> the orientation of the Cr moment along the chains overturns periodically with a consequent modulation of its modulus. The possible coexistence of alternating AFM-FM interactions between NN Cr<sup>3+</sup> atoms might be responsible for this peculiar behavior. The proposed magnetic structure is consistent with the observation that magnetic correlations in compounds similar to LiCrSe<sub>2</sub> display significant further neighbor interactions involving Cr–Cr distances of 6–7  $\text{\AA}$ <sup>22,26</sup>. Additionally, our results are in very good agreement with the findings of Kobayashi *et al.*<sup>35</sup>, who observed an AFM

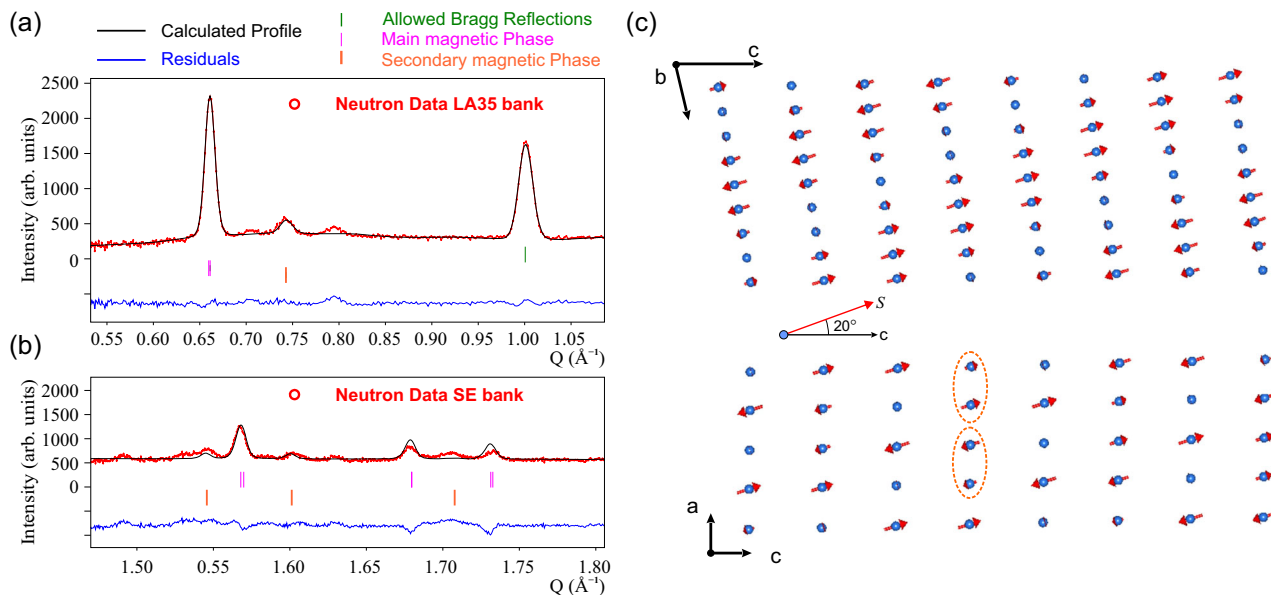


**Fig. 7** NPD results for the secondary magnetic phase in  $\text{LiCrSe}_2$ . Measured neutron diffraction pattern at  $T = 2$  K (red circles) with the corresponding calculated pattern (black continuous line) resulting from magnetic refinement for the two detector banks (a) low-Q LA35 and (b) intermediate-Q SE, respectively. Both the main (magenta) and secondary (orange) magnetic phases are characterized by vertical tick bars of different color. c Pictorial representation of the spin structure for the secondary magnetic structure. See also Supplementary Table 1 for the values of the refined parameters.

character of the signal in magnetic susceptibility measurements. This suggested that further neighbor exchange interactions in  $\text{LiCrSe}_2$  are in fact stronger than the nearest neighbor ones and of utmost importance in the determination of the magnetic ground state of  $\text{LiCrSe}_2$ . In reference<sup>35</sup> it was also hypothesized that  $\text{LiCrSe}_2$  is likely to possess a magnetic ground state different from other triangular lattice Cr chalcogenides with a similar structure and behavior<sup>21,22,26</sup>. The results of our work confirm this conjecture and provide a qualitative explanation for the difference between  $\text{LiCrSe}_2$  and the other systems: in  $\text{AuCrS}_2$  and  $\text{AgCrS}_2$  and  $\text{CuCrS}_2$  the in-plane Cr–Cr distances are always 3–4% different from the critical value found by Rosenberg. On the other hand, for  $\text{LiCrSe}_2$  the in-plane Cr–Cr distances are just  $\approx 1\%$  different from the critical value  $3.6$  Å. The Cr–Anion–Cr angles are very close to  $90^\circ$  in all cases. Therefore, in  $\text{LiCrSe}_2$  distinctive geometric conditions are realized, which lead to a configuration of the overlapping electronic orbitals that might allow the conflictual coexistence of FM and AFM exchange interactions over the same crystallographic sites, making this material unique in the 2D-TLA family. Future modeling efforts would be needed to systematically understand the complex spin interactions and order in  $\text{LiCrSe}_2$ . The detailed information presented in this work, concerning the atomic/spin arrangement across the transition, will most likely be a valuable input for such modeling efforts.

Going back to the un-indexed weak Bragg peaks found in the low-temperature  $C2/m$  phase, it is important to emphasize that we clearly do not believe that these peaks are from an impurity phase. This is because there is no trace of magnetic impurities in the room temperature diffraction patterns, there is no sign of phase separation in the wTF  $\mu^+$ SR data, and the additional peaks appear exactly at the same structural/magnetic transition temperature of the  $\text{LiCrSe}_2$  main phase ( $T_s = T_N = 30$  K). In our refinement efforts, a huge number of different magnetic propagation vectors in combination with different crystal structures and super-cells, including higher-order harmonics of the parent cell, were attempted for the purpose of simultaneous indexing of all the peaks in the diffraction pattern. Attempts of indexing the magnetic peaks with a single  $2q$  structure have been made and,

although the peak position could be retrieved in the refinement, the intensity of the calculated magnetic peaks could not match the intensity of the measured peaks. In order to identify a possible lower than  $C2/m$  symmetry for the nuclear structure, many attempts of indexing the nuclear peaks together with the small satellites have been made. Such attempts provided no solution. Attempts to refine the small satellites alone as an independent nuclear structure could not provide any solution either.

Therefore, these efforts did not produce any outcome and, even if the  $C2/m$  nuclear structure combined with magnetic propagation vector  $\mathbf{q}_{\text{main}}$  gives a very nice result, a few weak Bragg peaks were still left un-indexed [e.g.  $Q = 0.74$  Å<sup>-1</sup> being the strongest un-indexed peak, see Fig. 4a and Fig. 5b]. Considering the coinciding structural and magnetic phase transition occurring at  $T \approx 30$  K, it is indeed challenging to identify whether new Bragg peaks appearing at low temperature have nuclear or magnetic origin. In this work, we therefore combined NPD with synchrotron XRD experiments in order to improve the identification process. Indeed, the low-temperature peak at  $Q = 0.74$  Å<sup>-1</sup> is not visible in the  $T = 11$  K XRD data. This fact, together with the ZF  $\mu^+$ SR results indicating the presence of two slightly different magnetic phases, and with the low-Q position and temperature-dependent behavior of the satellites in the ND pattern, seems to point toward a magnetic nature for these peaks. For this reason, we decided to try to index the few weak remaining low-temperature satellites with a secondary magnetic phase. Considering the fact that the ZF asymmetry of the the first Bessel component,  $A_{\text{Bess1}}$ , was so much smaller than  $A_{\text{Bess2}}$ , it seems reasonable to assume that the weak un-indexed magnetic Bragg peaks could be associated with  $A_{\text{Bess1}}$ .

To deduce the possible secondary magnetic phase (consistent with the presence of a magnetic supercell) we utilized a similar procedure as for the identification of the main magnetic structure. The refinement [Fig. 7a, b], carried out with a global routine taking into account all the detector banks, successfully provided a good match for both position and intensity of most of the minority satellites [orange tick-marks in Fig. 7a, b]. The resulting secondary magnetic structure, characterized by an

incommensurate propagation vector  $\mathbf{q}_{\text{secondary}} = (0.7249(5), -0.0885(3), -0.1292(9))$ , appears similar yet complementary to the main structure, although in this case the spin axial vector forms a canting angle of about  $20^\circ$  with the  $c$ -axis. Here the canted modulated FM chains run along the  $c$ -axis while the up-up-down-down arrangement of the Cr spins develops along the  $a$ -axis [Fig. 7c]. A more detailed description of this refinement can be found in the Supplementary Information.

A magnetic nature for the minority satellites would be consistent with the results of the ZF  $\mu^+$ SR, also considering the ratio between the two phases. Moreover, the clear canting angle found in the secondary magnetic phase is suggestive of the presence of asymmetric magnetic couplings, possibly due to the presence of Dzyaloshinskii–Moriya interaction (DMI). This would be consistent with a recent theoretical work<sup>36</sup>, which indeed predicts the occurrence of large DMI in LiCrSe<sub>2</sub>. However, the reliability  $R$ -factor for the refinement of the secondary magnetic phase has a rather large value ( $R_{\text{B(mag)}}^{\text{secondary}} = 25.7\%$ ), implying a relatively poor agreement between the experimental data and the calculated model for this phase. The large value for the  $R$ -factor, although it could simply be due to the scarcity and weak intensity of the refined satellites, makes this interpretation for the nature of the minority satellites not fully unambiguous. Therefore, another option might be that the small un-indexed low-temperature Bragg peaks are in fact not magnetic but have nuclear origin related to charge ordering. Indeed, we could consider the appearance of a superstructure induced by e.g. Li(-vacancy) ordering. In principle such superstructure peaks should be visible also in the XRD, however, if they are indeed originating from the light Li atoms (low  $Z$ ) the peaks might be difficult to discern (or even invisible) for X-rays. Possible indications of the validity of this option could be found in the high-temperature properties of LiCrSe<sub>2</sub> [Fig. 6].

The dynamic phenomenology manifested by LiCrSe<sub>2</sub> is reminiscent of the behavior of the rather well-known and strongly related Na <sub>$x$</sub> CoO<sub>2</sub> (NCO) compound<sup>2–6</sup>. From very extensive studies of NCO it has been shown that Na-ions (vacancies) can order in many different types of configurations<sup>70–72</sup>. It was also clearly shown that the Na-ion are in fact mobile even below room temperature and that the dynamics allow the Na-ions to arrange themselves in different patterns at lower temperatures<sup>5,73,74</sup>. Even in the case of NCO with the heavier Na-ions, it was not straightforward to identify the superstructure ordering. Several of the successful studies were performed using neutron scattering and, in more or less all cases, the superstructures could only be identified using single crystalline samples rather than powder. It was also in single crystals where the most recent study of the in-plane as well as out-of-plane Na ordering was studied, this time using XRD<sup>75</sup>. Therefore, in qualitative agreement with NCO, it is not improbable that the small satellites found in NPD on LiCrSe<sub>2</sub> could be nuclear superstructures and still not visible in the XRD pattern. However, NCO and LiCrSe<sub>2</sub> present some differences: in NCO there are two Na sites and neither of them is fully occupied, while in LiCrSe<sub>2</sub> there is only one Li site, which results fully occupied from our refinement (i.e. no vacancies). On the other hand, the refined magnetic (main) phase has a very long periodicity (large unit cell), which would fit well with a Li-vacancy order based on very few existing vacancies that we did not discern in our refinement. It is of course possible to have Li order without vacancies, e.g. in the form of a charge-density-wave (CDW), but future more detailed studies of Li-ion ordering and dynamics in LiCrSe<sub>2</sub> coupled to the magnetic properties would be needed to clarify this aspect.

Finally, we speculate about the electronic origins of the magnetic peaks and the very unusual spin arrangement realized in

LiCrSe<sub>2</sub>. The spin density modulation along the FM chains and the incommensurate positions of the magnetic peaks might be originated by a combination of localized and itinerant moments, with a phenomenology similar to both the Na <sub>$x$</sub> CoO<sub>2</sub> compound<sup>76</sup> as well as the intermetallic material ErPd<sub>2</sub>Si<sub>2</sub>. The latter in fact also manifests two distinct incommensurate spin states<sup>77</sup>. Looking at the size of the magnetic peaks belonging to the two structures, it can be argued that the moments for  $\mathbf{q}_{\text{main}}$  have mostly a localized character, while  $\mathbf{q}_{\text{secondary}}$  are mainly itinerant. Although being consistent with the experimental observations, single crystal magnetic field-dependent studies would be necessary to confirm or deny such hypothesis. On the other hand, the comparison with NCO actually opens up an even more interesting possibility. Considering that both LiCrSe<sub>2</sub> and NCO have their magnetic ions sitting on the triangular (frustrated) lattice with competing magnetic interactions, the spins are highly susceptible to any additional perturbation. In the case of NCO it was clearly shown that the Na-ion ordering actually creates a periodic coulomb potential (charge) landscape that is able to tune the electronic states and magnetic properties within the TMO layers<sup>76</sup>. It has even been proved that, by controlling the cooling rate of the sample, thereby gaining control of dynamics and vacancy order, different magnetic ground states could be achieved for the NCO compound<sup>4,75</sup>. Further, by electrochemical cycling of NCO inside a battery cell (i.e. changing the Na content  $x$  for Na <sub>$x$</sub> CoO<sub>2</sub>), very detailed studies could be performed on the nuclear structure<sup>78</sup> as well as how this strongly affects the magnetic phase diagram<sup>6,79</sup>. The conditions for such phenomenology could in fact be verified also for LiCrSe<sub>2</sub>. We could imagine that if Li-ions organize themselves in an ordered pattern, their periodic potential could affect the spin order within the triangular lattice Cr planes. Such effect could be the origin for the peculiar main magnetic phase ( $\mathbf{q}_{\text{main}}$ ) firmly established in LiCrSe<sub>2</sub>, as well as for the potential secondary magnetic cell ( $\mathbf{q}_{\text{secondary}}$ ).

In summary, we discuss a few possible scenarios attempting to explain the un-indexed Bragg peaks found in our NPD data. Here it is important to underline that, although neutron powder diffraction is a powerful technique for studying crystal and magnetic structures, it does have some limitations, especially when dealing with complex systems. NPD provides average structural information from a polycrystalline sample, but not detailed information about single crystal domains or orientation-dependent properties. In complex systems, there may be significant peak overlap in the diffraction pattern, making it difficult to assign individual reflections to specific structural or magnetic components. Indeed, neutron powder diffraction typically has lower resolution compared to single crystal diffraction techniques, which can limit the precise determination of complex structural features. Symmetry-equivalent reflections will have the same  $d$ -spacing, therefore, especially in case of coexistence of multiple phases, the resulting powder diffraction pattern can be challenging to interpret accurately. This difficulty applies also to the determination of complex magnetic structures involving multiple magnetic substructures. Background signals and sample absorption can also interfere with weak diffraction peaks, especially in magnetic systems with low scattering strength.

These limitations can be mitigated in several ways, such as the ones adopted in this work. High-resolution TOF powder diffraction instruments and carefully optimized experimental conditions can help reduce peak overlap, resolve fine structural details, and capture the system's behavior in a broad  $Q$ -range at all relevant conditions. Additionally, by combining data from multiple techniques like synchrotron X-ray diffraction and muon spin rotation, peak assignment can be improved leading to an enhanced accuracy of the solution. The analysis of the secondary



phases can be conducted separately, which allows to disentangle their respective contributions to the diffraction pattern. Also in this case, the combination of neutron powder diffraction with other characterization techniques aids in resolving phase separation issues. Using high-quality samples can also significantly improve the reliability and accuracy of the structural determination and help overcome some of the challenges associated with this technique. A high-quality sample with a well-defined crystallinity, homogeneity and purity ensures a better signal-to-noise ratio, a more reliable average representation of the entire sample, as well as sharper and well resolved diffraction peaks in the pattern, facilitating peak assignment.

For these reasons, despite the inherent limitations of NPD, our solution for the magnetic phase in LiCrSe<sub>2</sub> is overall a reasonably good representation of the magnetic ordering in this material. The uncertainty about the nature of the minority satellites can be removed by complementing the powder diffraction data with single crystal diffraction data, which can help resolve possible structural and magnetic ambiguities in the powder pattern.

In this regard, to ultimately discern if the additional satellites are of nuclear or magnetic origin, single crystal polarized neutron diffraction would be the optimal approach. However, although single crystal synthesis of the related compound LiCrTe<sub>2</sub> has been very recently successfully achieved<sup>80</sup>, to the best of our knowledge no large enough LiCrSe<sub>2</sub> single crystals are presently available.

## Conclusions

The magnetic and crystal structure of the triangular antiferromagnet LiCrSe<sub>2</sub> has been solved at high and low temperature by means of neutron diffraction, synchrotron X-ray diffraction and muon spin rotation experimental techniques. The unique arrangement of the Cr atoms in this material is consistent with the simultaneous presence of competing nearest-neighbor ferromagnetic and antiferromagnetic exchange couplings over the same crystallographic sites, with a predominance of the next nearest neighbor interactions in the determination of the magnetic ground state in LiCrSe<sub>2</sub>. As a result, a structural transition from trigonal *P*3̄*m*1 to monoclinic *C*2/*m* crystal system induced by a strong magnetoelastic coupling occurs, accompanied by the formation of two up-up-down-down magnetic structures (a main one and a secondary one) with itinerant modulation of the Cr spin axial vector, in direction and modulus, and incommensurate *q* – vectors  $\mathbf{q}_{\text{main}} = (0.045, \approx \frac{1}{4}, \approx \frac{1}{2})$  and  $\mathbf{q}_{\text{secondary}} = (0.7249(5), -0.0885(3), -0.1292(9))$ . Such arrangement of the Cr spins is reminiscent of the magnetic ordering established in the Cr sulfide triangular antiferromagnets AuCrS<sub>2</sub> and AgCrS<sub>2</sub> which also manifest strong magnetoelastic coupling. However, the seemingly unprecedented geometric conditions realized in LiCrSe<sub>2</sub> provide access to a unique combination of the competing magnetic mechanisms, resulting in a much more complex magnetic ground state in which the magnetic moment is periodically suppressed and changes direction. This peculiar behavior might be originated from a dual itinerant/localized nature of the electrons in this system. From the results of this work LiCrSe<sub>2</sub> was proven to be an extremely fascinating study case, which lends itself to very promising future single crystal investigations, and constitutes an important step forward in understanding the spin-lattice relationship in strongly correlated spin systems.

## Methods

Polycrystalline LiCrSe<sub>2</sub> was prepared by direct reaction of the Li, Cr, and Se elements. The sample preparation is described in higher detail in reference<sup>35</sup>.

**Bulk  $\mu^+$ SR Experiment.** The temperature-dependent bulk- $\mu^+$ SR spectra have been acquired at the multi purpose muon beam-line M20 of Canada's particle accelerator center TRIUMF. ~200 mg of LiCrSe<sub>2</sub> in powder was packed in a 1 × 1 cm<sup>2</sup> area Aluminum-coated Mylar tape (0.05 mm thickness), in order to reduce the background signal. This envelope was attached to a low background sample holder inserted in a helium exchange gas cryostat (temperature range: 2 K to 300 K).

**LF- $\mu^+$ SR experiment.** The high-temperature LF- $\mu^+$ SR data were obtained using the surface muon beamline S1 at the high-intensity proton accelerator facility J-PARC, in Japan. The LiCrSe<sub>2</sub> powder was pressed into a pellet introduced into hermetically sealed non-magnetic titanium cells. The surface of the pellet facing the muon beam was covered using a very thin (50  $\mu\text{m}$ ) titanium window. By using a closed-cycle refrigerator (CCR), data were collected in the temperature range  $T = 50 - 375$  K. A more detailed description of the sample cell and experimental setup can be found in ref. <sup>56</sup>.

**Synchrotron XRD experiment.** The XRD measurements were collected at the instrument I11 of the Diamond Light Source in Didcot (UK). The sample was mounted by filling and sealing an Al capillary with internal diameter 0.7 mm, which was in turn attached to a phoenix cryostat, with a 10° sample rocking stage, which allows measurements in a temperature range from 11 K to 300 K.

**Neutron diffraction experiment.** The time-of-flight (ToF) neutron diffraction measurements were performed at the powder diffractometer iMATERIA<sup>81</sup>, at J-PARC, in Japan. The powder samples (~500 mg) were mounted into cylindrical vanadium cells with diameters and 5 mm and sealed with an aluminum cap, aluminum screws and indium wire. The cell was mounted on a closed cycle refrigerator to reach temperatures between 2 K and 300 K. iMATERIA allows for the simultaneous adoption of different detector banks for wide d-range (Q-range) coverage. The backscattering bank (BS), suitable for detailed structural characterization, has a resolution  $\Delta d/d = 0.16\%$  and covers a d-range from 0.181 Å up to 5.09 Å. The 90-degree detector bank (SE) has a resolution  $\Delta d/d = 0.5\%$  and covers a d-range from 0.255 Å up to 7.2 Å. The low angle bank (LA35), ideal for the detection of low Q-range magnetic Bragg peaks, has a d-range from 0.25 Å up to 40 Å.

The sample preparations for all the measurements were carried out in a controlled environment using Ar and/or He glove-boxes, to avoid degradation of the highly air- and moisture-sensitive LiCrSe<sub>2</sub> samples.

**Softwares.** The crystal and magnetic structure determination was carried out with the help of the Bilbao crystallographic server<sup>82,83</sup>, and the FullProf software suite<sup>84</sup> was employed for the data refinement. All images involving crystal structure were made with the VESTA software<sup>85</sup>, the parameter plots and fitting are produced with the software Igorpro<sup>86</sup> and the  $\mu^+$ SR data were fitted using the software package *musrfit*<sup>87</sup>.

## Data availability

All the data of this work are available from the corresponding authors on request. The data are also publicly available on request from the repositories of the respective large-scale facilities where the experiments were performed upon providing the experimental beam time proposal number (see acknowledgements).

Received: 13 January 2023; Accepted: 20 September 2023;

Published online: 07 October 2023



## References

- Anderson, P. W. Resonating valence bonds: a new kind of insulator? *Mater. Res. Bull.* **8**, 153–160 (1973).
- Sugiyama, J. et al. Static magnetic order in  $\text{Na}_{0.75}\text{CoO}_2$  detected by muon spin rotation and relaxation. *Phys. Rev. B* **67**, 214420 (2003).
- Hertz, J. T. et al. Magnetism and structure of  $\text{Li}_x\text{CoO}_2$  and comparison to  $\text{Na}_x\text{CoO}_2$ . *Phys. Rev. B* **77**, 075119 (2008).
- Schulze, T. F. et al. Direct link between low-temperature magnetism and high-temperature sodium order in  $\text{Na}_x\text{CoO}_2$ . *Phys. Rev. Lett.* **100**, 026407 (2008).
- Medarde, M. et al. 1D to 2D  $\text{Na}^+$  ion diffusion inherently linked to structural transitions in  $\text{Na}_{0.7}\text{CoO}_2$ . *Phys. Rev. Lett.* **110**, 266401 (2013).
- Sassa, Y. et al. Investigation of the magnetic properties of  $\text{Na}_{0.7}\text{CoO}_2$  prepared by electrochemical reaction. *JPS Conf. Proc.* **21**, 011019 (2018).
- Sugiyama, J. et al. Nuclear magnetic field in  $\text{Na}_{0.7}\text{CoO}_2$  detected with  $\mu$ -SR. *Phys. Rev. B* **102**, 144431 (2020).
- Soubeyroux, J., Fruchart, D., Delmas, C. & Flem, G. L. Neutron powder diffraction studies of two-dimensional magnetic oxides. *J. Magn. Magn. Mater.* **14**, 159–162 (1979).
- Sugiyama, J. et al.  $\mu$ +SR investigation of local magnetic order in  $\text{LiCrO}_2$ . *Phys. Rev. B* **79**, 184411 (2009).
- Pen, H., Van Den Brink, J., Khomskii, D. & Sawatzky, G. Orbital ordering in a two-dimensional triangular lattice. *Phys. Rev. Lett.* **78**, 1323 (1997).
- Katayama, N. et al. Anomalous metallic state in the vicinity of metal to valence-bond solid insulator transition in  $\text{LiVS}_2$ . *Phys. Rev. Lett.* **103**, 146405 (2009).
- McQueen, T. et al. Successive orbital ordering transitions in  $\text{NaVO}_2$ . *Phys. Rev. Lett.* **101**, 166402 (2008).
- Takada, K. et al. Superconductivity in two-dimensional  $\text{CoO}_2$  layers. *Nature* **422**, 53–55 (2003).
- Neupert, T., Denner, M. M., Yin, J.-X., Thomale, R. & Hasan, M. Z. Charge order and superconductivity in Kagome materials. *Nat. Phys.* **18**, 137–143 (2022).
- Palmer, R. G., Stein, D. L., Abrahams, E. & Anderson, P. W. Models of hierarchically constrained dynamics for glassy relaxation. *Phys. Rev. Lett.* **53**, 958 (1984).
- Terada, N. et al. Spiral-spin-driven ferroelectricity in a multiferroic delafossite  $\text{AgFeO}_2$ . *Phys. Rev. Lett.* **109**, 097203 (2012).
- Arh, T. et al. The Ising triangular-lattice antiferromagnet neodymium heptatantalate as a quantum spin liquid candidate. *Nat. Mater.* **21**, 416–422 (2022).
- Tóth, S. et al. Electromagnon dispersion probed by inelastic x-ray scattering in  $\text{LiCrO}_2$ . *Nat. Commun.* **7**, 13547 (2016).
- Ji, S. et al. Spin-lattice order in frustrated  $\text{ZnCr}_2\text{O}_4$ . *Phys. Rev. Lett.* **103**, 037201 (2009).
- Oh, J. et al. Magnon breakdown in a two dimensional triangular lattice heisenberg antiferromagnet of multiferroic  $\text{LuMnO}_3$ . *Phys. Rev. Lett.* **111**, 257202 (2013).
- Rasch, J. C. et al. Magnetoelastic coupling in the triangular lattice antiferromagnet  $\text{CuCrS}_2$ . *Phys. Rev. B* **80**, 104431 (2009).
- Carlsson, S. et al. Suppression of geometric frustration by magnetoelastic coupling in  $\text{AuCrS}_2$ . *Phys. Rev. B* **84**, 094455 (2011).
- Lopes, A. et al. Local distortions in multiferroic  $\text{AgCrO}_2$  triangular spin lattice. *Phys. Rev. B* **84**, 014434 (2011).
- Van Laar, B. & Ijdo, D. Preparation, crystal structure, and magnetic structure of  $\text{LiCrS}_2$  and  $\text{LiVS}_2$ . *J. Solid State Chem.* **3**, 590–595 (1971).
- Engelsman, F., Wiegers, G., Jellinek, F. & Van Laar, B. Crystal structures and magnetic structures of some metal (I) chromium (III) sulfides and selenides. *J. Solid State Chem.* **6**, 574–582 (1973).
- Damay, F. et al. Magnetoelastic coupling and unconventional magnetic ordering in the multiferroic triangular lattice  $\text{AgCrS}_2$ . *Phys. Rev. B* **83**, 184413 (2011).
- Van Laar, B. & Engelsman, F. The magnetic structure of  $\text{KCrS}_2$ . *J. Solid State Chem.* **6**, 384–386 (1973).
- Hartmann, O. et al. Magnetic properties of the multiferroic chromium thio-spinels  $\text{CdCr}_2\text{S}_4$  and  $\text{HgCr}_2\text{S}_4$ . *Eur. Phys. J. B* **86**, 148 (2013).
- Halley, D. et al. Size-induced enhanced magnetoelectric effect and multiferroicity in chromium oxide nanoclusters. *Nat. Commun.* **5**, 3167 (2014).
- Soda, M. et al. Continuous control of local magnetic moment by applied electric field in multiferroics  $\text{Ba}_2\text{CoGe}_2\text{O}_7$ . *Phys. Rev. B* **94**, 094418 (2016).
- Bazazzadeh, N. et al. Magnetoelastic coupling enabled tunability of magnon spin current generation in two-dimensional antiferromagnets. *Phys. Rev. B* **104**, L180402 (2021).
- Grimes, C. A., Roy, S. C., Rani, S. & Cai, Q. Theory, instrumentation and applications of magnetoelastic resonance sensors: a review. *Sensors* **11**, 2809–2844 (2011).
- Saiz, P. G., de Luis, R. F., Lasheras, A., Arriortua, M. I. & Lopes, A. C. Magnetoelastic resonance sensors: principles, applications, and perspectives. *ACS Sensors* **7**, 1248–1268 (2022).
- Kobayashi, S., Ueda, H., Nishio-Hamane, D., Michioka, C. & Yoshimura, K. Successive phase transitions driven by orbital ordering and electron transfer in quasi-two-dimensional  $\text{CrSe}_2$  with a triangular lattice. *Phys. Rev. B* **89**, 054413 (2014).
- Kobayashi, S., Ueda, H., Michioka, C. & Yoshimura, K. Competition between the direct exchange interaction and superexchange interaction in layered compounds  $\text{LiCrSe}_2$ ,  $\text{LiCrTe}_2$ , and  $\text{NaCrTe}_2$  with a triangular lattice. *Inorg. Chem.* **55**, 7407–7413 (2016).
- Li, P., Cui, Q., Ga, Y., Liang, J. & Yang, H. Large Dzyaloshinskii-Moriya interaction and field-free topological chiral spin states in two-dimensional alkali-based chromium chalcogenides. *Phys. Rev. B* **106**, 024419 (2022).
- Xu, W., Ali, S., Jin, Y., Wu, X. & Xu, H. Intrinsic ferromagnetic semiconductors in two-dimensional alkali-based chromium chalcogenides. *ACS Appl. Electron. Mater.* **2**, 3853–3858 (2020).
- Kumari, S., Pradhan, D. K., Pradhan, N. R. & Rack, P. D. Recent developments on 2D magnetic materials: challenges and opportunities. *Emergent Mater.* **4**, 827–846 (2021).
- Kobayashi, S. et al. Linear trimer formation with antiferromagnetic ordering in 1T- $\text{CrSe}_2$  originating from Peierls-like instabilities and interlayer Se–Se interactions. *Inorg. Chem.* **58**, 14304–14315 (2019).
- Blundell, S. Spin-polarized muons in condensed matter physics. *Contemp. Phys.* **40**, 175–192 (1999).
- Nocerino, E. et al. Nuclear and magnetic spin structure of the antiferromagnetic triangular lattice compound  $\text{LiCrTe}_2$  investigated by  $\mu$ +SR, neutron and x-ray diffraction. *Sci. Rep.* **12**, 21657 (2022).
- Sugiyama, J. et al. Pressure dependence of ferromagnetic phase boundary in  $\text{BaVSe}_3$  studied with high-pressure  $\mu$ +SR. *Phys. Rev. B* **103**, 104418 (2021).
- Nocerino, E. et al. Magnetic nature of wolframite  $\text{MgReO}_4$ . *J. Phys.: Conf. Ser.* **2462**, 012037 (2023).
- Nocerino, E. et al. Unusually large magnetic moment and tricritical behavior of the cmr compound  $\text{NaCr}_2\text{O}_4$  revealed with high resolution neutron diffraction and  $\mu$ +SR. *J. Phys.: Mater.* **6**, 035009 (2023).
- Major, J. et al. Zero-field muon spin rotation in monocrystalline chromium. *Hyperfine Interact.* **31**, 259–264 (1986).
- Amato, A. et al. Muon-spin-relaxation studies on the heavy-fermion system with non-fermi-liquid behavior  $\text{CeCu}_{5.9}\text{Au}_{0.1}$ . *Phys. Rev. B* **52**, 54 (1995).
- Andreica, D. Magnetic phase diagram in some Kondo-Lattice compounds: Microscopic and macroscopic studies. Ph.D. thesis, IPP/ETH-Zurich (2001).
- Lovesey, S. W. *Theory of Neutron Scattering from Condensed Matter: Volume II: Polarization Effects and Magnetic Scattering. Theory of Neutron Scattering from Condensed Matter* (Clarendon Press, 1986).
- Ivantchev, S., Kroumova, E., Madariaga, G., Perez-Mato, J. & Aroyo, M. SUBGROUPGRAPH: a computer program for analysis of group-subgroup relations between space groups. *J. Appl. Crystallogr.* **33**, 1190–1191 (2000).
- Rosenberg, M., Knülle, A., Sabrowsky, H. & Platte, C. Magnetic properties and structure of some ternary chromium chalcogenides with thallium and silver. *J. Phys. Chem. Solids* **43**, 87–95 (1982).
- Wills, A. Magnetic structures and their determination using group theory. *J. Physique IV* **11**, Pr9–133 (2001).
- Streltsov, S. V. & Khomskii, D. I. Covalent bonds against magnetism in transition metal compounds. *Proc. Natl Acad. Sci.* **113**, 10491–10496 (2016).
- Khatua, J. et al. Magnetic properties of the triangular-lattice antiferromagnets  $\text{Ba}_2\text{RB}_3\text{O}_{18}$  ( $R = \text{Yb, Er}$ ). *Phys. Rev. B* **106**, 104408 (2022).
- Schmidt, B. & Thalmeier, P. Frustrated two dimensional quantum magnets. *Phys. Rep.* **703**, 1–59 (2017).
- Nozaki, H. et al. Incommensurate spin-density-wave order in quasi-one-dimensional metallic antiferromagnet  $\text{NaV}_2\text{O}_4$ . *Physical Review B* **81**, 100410(R) (2010).
- Matsubara, N. et al. Magnetism and ion diffusion in honeycomb layered oxide  $\text{K}_2\text{Ni}_2\text{TeO}_6$ . *Sci. Rep.* **10**, 18305 (2020).
- Baenitz, M. et al. Planar triangular  $S = 3/2$  magnet  $\text{AgCrSe}_2$ : Magnetic frustration, short range correlations, and field-tuned anisotropic cycloidal magnetic order. *Phys. Rev. B* **104**, 134410 (2021).
- Mizushima, K., Jones, P., Wiseman, P. & Goodenough, J.  $\text{Li}_x\text{CoO}_2$  ( $0 < x < 1$ ): A new cathode material for batteries of high energy density. *Mater. Res. Bull.* **15**, 783–789 (1980).
- Xie, J. & Lu, Y.-C. A retrospective on lithium-ion batteries. *Nat. Commun.* **11**, 2499 (2020).
- Sugiyama, J. et al. Li diffusion in  $\text{Li}_x\text{CoO}_2$  probed by muon-spin spectroscopy. *Phys. Rev. Lett.* **103**, 147601 (2009).
- Månsson, M. & Sugiyama, J. Muon-spin relaxation study on li- and Na-diffusion in solids. *Phys. Scr.* **88**, 068509 (2013).
- Blundell, S. J., De Renzi, R., Lancaster, T. & Pratt, F. L. (eds.) *Muon Spectroscopy* (Oxford University Press, 2021).
- Campbell, I. Frustrated itinerant magnetism. *Braz. J. Phys.* **25**, 295–301 (1995).
- Li, B. et al. Competing magnetic phases and itinerant magnetic frustration in  $\text{SrCo}_2\text{As}_2$ . *Phys. Rev. B* **100**, 054411 (2019).

65. Goodenough, J. & Loeb, A. Theory of ionic ordering, crystal distortion, and magnetic exchange due to covalent forces in spinels. *Phys. Rev.* **98**, 391 (1955).
66. Kanamori, J. Superexchange interaction and symmetry properties of electron orbitals. *J. Phys. Chem. Solids* **10**, 87–98 (1959).
67. Anderson, P. W. Antiferromagnetism. theory of superexchange interaction. *Phys. Rev.* **79**, 350 (1950).
68. Ushakov, A., Kukusta, D., Yaresko, A. & Khomskii, D. Magnetism of layered chromium sulfides  $M\text{CrS}_2$  ( $M = \text{Li, Na, K, Ag, and Au}$ ): a first-principles study. *Phys. Rev. B* **87**, 014418 (2013).
69. Komleva, E. V., Irkhin, V. Y., Solovyev, I. V., Katsnelson, M. I. & Streltsov, S. V. Unconventional magnetism and electronic state in the frustrated layered system  $\text{pdcro 2}$ . *Phys. Rev. B* **102**, 174438 (2020).
70. Roger, M. et al. Patterning of sodium ions and the control of electrons in sodium cobaltate. *Nature* **445**, 631–634 (2007).
71. Morris, D. J. P. et al. Crystal-to-stripe reordering of sodium ions in  $\text{Na}_x\text{CoO}_2$  ( $x \geq 0.75$ ). *Phys. Rev. B* **79**, 100103(R) (2009).
72. Meng, Y. S., Hinuma, Y. & Ceder, G. An investigation of the sodium patterning in  $\text{Na}_x\text{CoO}$  ( $0.5 < x < 1$ ) by density functional theory methods. *J. Chem. Phys.* **128**, 104708 (2008).
73. Weller, M., Sacchetti, A., Ott, H. R., Mattenberger, K. & Batlogg, B. Melting of the Na Layers in Solid  $\text{Na}_{0.8}\text{CoO}_2$ . *Phys. Rev. Letters* **102**, 056401 (2009).
74. Willis, T. J. et al. Diffusion mechanism in the sodium-ion battery material sodium cobaltate. *Sci. Rep.* **8**, 3210 (2018).
75. Galeski, S., Mattenberger, K. & Batlogg, B. Interplay between magnetism and sodium vacancy ordering in  $\text{Na}_x\text{CoO}_2$ . *Phys. Rev. B* **94**, 140402(R) (2016).
76. Julien, M.-H. et al. Electronic texture of the thermoelectric oxide  $\text{Na}_{0.75}\text{CoO}_2$ . *Phys. Rev. Lett.* **100**, 096405 (2008).
77. Li, H.-F. et al. Distinct itinerant spin-density waves and local-moment antiferromagnetism in an intermetallic  $\text{ErPd}_2\text{Si}_2$  single crystal. *Sci. Rep.* **5**, 1–7 (2015).
78. Berthelot, R., Carlier, D. & Delmas, C. Electrochemical investigation of the  $\text{P2-Na}_x\text{CoO}_2$  phase diagram. *Nat. Mater.* **10**, 74–80 (2010).
79. Foo, M. L. et al. Charge ordering, commensurability, and metallicity in the phase diagram of the layered  $\text{Na}_x\text{CoO}_2$ . *Phys. Rev. Lett.* **92**, 247001 (2004).
80. Witteveen, C. et al. Synthesis and anisotropic magnetic properties of  $\text{LiCrTe}$  single crystals with a triangular-lattice antiferromagnetic structure. *J. Phys.: Mater.* **6**, 035001 (2023).
81. Ishigaki, T. et al. IBARAKI materials design diffractometer (iMATERIA)-versatile neutron diffractometer at J-PARC. *Nucl. Instrum. Methods Phys. Res. A: Accelerators Spectrom. Detectors Assoc. Equipment* **600**, 189–191 (2009).
82. Aroyo, M. I. et al. Bilbao crystallographic server: I. databases and crystallographic computing programs. *Z. Kristallogr.-Crystalline Mater.* **221**, 15–27 (2006).
83. Aroyo, M. I., Kirov, A., Capillas, C., Perez-Mato, J. & Wondratschek, H. Bilbao crystallographic server. II. representations of crystallographic point groups and space groups. *Acta Crystallogr. A: Foundations. Crystallogr.* **62**, 115–128 (2006).
84. Rodríguez-Carvajal, J. Recent advances in magnetic structure determination by neutron powder diffraction. *Phys. B: Condens. Matter* **192**, 55–69 (1993).
85. Momma, K. & Izumi, F. VESTA: a three-dimensional visualization system for electronic and structural analysis. *J. Appl. Crystallogr.* **41**, 653–658 (2008).
86. WaveMetrics. IGOR Pro, Scientific Data Analysis Software (2016). <http://www.wavemetrics.com/products/igorpro/igorpro.htm>
87. Suter, A. & Wojek, B. M. Musrfit: A free platform-independent framework for  $\mu\text{SR}$  data analysis. *Phys. Proc.* **30**, 69 (2012).

## Acknowledgements

The  $\mu^+\text{SR}$  measurements were performed at the instrument M20 of the muon source TRIUMF (beam time proposal: M1673) as well as at the S1 beam line of J-PARC (beam time proposal: 2019A0327). The XRD measurements were performed at the instrument I11 of the synchrotron facility Diamond (beam time proposal: CY23840). The NPD measurements were performed at the instrument iMATERIA of the neutron spallation source J-PARC (beam time proposal: 20180056A). The authors wish to thank Hiroshi

Nozaki for his support during the  $\mu^+\text{SR}$  experiment, and Juan Rodríguez-Carvajal for the assistance he provided on the neutron diffraction data refinement, along with the staff of TRIUMF, Diamond and J-PARC for the help in the experimental measurements. This research is funded by the Swedish Foundation for Strategic Research (SSF) within the Swedish national graduate school in neutron scattering (SwedNess), as well as the Swedish Research Council VR (Dnr. 2022-03936, Dnr. 2021-06157, and Dnr. 2017-05078), and the Carl Tryggers Foundation for Scientific Research (CTS-22:2374). J.S. is supported by the Japan Society for the Promotion Science (JSPS) KAKENHI Grant No. JP18H01863 and JP20K21149. Y.S. and O.K.F. acknowledge funding from the Swedish Research Council (VR) through a Starting Grant (Dnr. 2017-05078) and Area of Advances-Material Sciences from Chalmers University of Technology. Y.S. is also supported by Wallenberg Young Fellow through the grant KAW 2021.0150. S.K. and K.Y. are supported by JSPS KAKENHI Grant No.18KK0150. The work at the University of Zürich and the University of Geneva was supported by the Swiss National Science Foundation under Grant No. PCEFP2-194183.

## Author contributions

E.N., J.S., and M.M. conceived the experiments. E.N., O.K.F., N.M., C.T., T.M., A.H., A.K., I.U., Y.S., J.S., and M.M. conducted the experiments. E.N., J.S., N.M., O.K.F., J.H.B., V.P., and M.M. analyzed the results. The samples were synthesized by S.K. and K.Y., as well as by C.W. and F.O.v.R.; they also conducted the initial sample characterizations. E.N. and M.M. made all the figures. E.N. created the first draft, and all co-authors reviewed and revised the manuscript.

## Funding

Open access funding provided by Royal Institute of Technology.

## Competing interests

The authors declare no competing interests.

## Additional information

**Supplementary information** The online version contains supplementary material available at <https://doi.org/10.1038/s43246-023-00407-x>.

**Correspondence** and requests for materials should be addressed to Elisabetta Nocerino or Martin Månsson.

**Peer review information** *Communications Materials* thanks the anonymous reviewers for their contribution to the peer review of this work. Primary Handling Editors: Alannah Hallas and Aldo Isidori.

**Reprints and permission information** is available at <http://www.nature.com/reprints>

**Publisher's note** Springer Nature remains neutral with regard to jurisdictional claims in published maps and institutional affiliations.



**Open Access** This article is licensed under a Creative Commons Attribution 4.0 International License, which permits use, sharing, adaptation, distribution and reproduction in any medium or format, as long as you give appropriate credit to the original author(s) and the source, provide a link to the Creative Commons licence, and indicate if changes were made. The images or other third party material in this article are included in the article's Creative Commons licence, unless indicated otherwise in a credit line to the material. If material is not included in the article's Creative Commons licence and your intended use is not permitted by statutory regulation or exceeds the permitted use, you will need to obtain permission directly from the copyright holder. To view a copy of this licence, visit <http://creativecommons.org/licenses/by/4.0/>.

© The Author(s) 2023, corrected publication 2023